52

NASA CR - 134685

8 cm TECHNOLOGY THRUSTER DEVELOPMENT

J. HYMAN, JR.

HUGHES RESEARCH LABORATORIES
A DIVISION OF HUGHES AIRCRAFT COMPANY
3011 MALIBU CANYON ROAD
MALIBU, CALIFORNIA 90265

PREPARED FOR

NATIONAL AERONAUTICS AND SPACE ADMINISTRATION
NASA LEWIS RESEARCH CENTER
CLEVELAND, OHIO 44135

W. R. HUDSON, NASA PROJECT MANAGER

CONTRACT NAS 3-17791

FINAL REPORT

JULY 1974

(NASA-CR-134685) EIGHT cm TECHNOLOGY
THRUSTER DEVELOPMENT Final Report
(Hughes Research Labs.) 93 p HC $7.75

CSCL 21C

N74-33227

Unclas
G3/28 48461

1. Report No. NASA CR-134685	2. Government Accession No.	3. Recipient's Catalog No.
4. Title and Subtitle 8-cm TECHNOLOGY THRUSTER DEVELOPMENT		5. Report Date July 1974
		6. Performing Organization Code
7. Author(s) Julius Hyman, Jr.		8. Performing Organization Report No.
		10. Work Unit No.
9. Performing Organization Name and Address Hughes Research Laboratories 3011 Malibu Canyon Road Malibu, California 90265		11. Contract or Grant No. NAS 3-17791
12. Sponsoring Agency Name and Address National Aeronautics and Space Administration Washington, D.C. 20546		13. Type of Report and Period Covered Final Technical Report July 1974
		14. Sponsoring Agency Code

15. Supplementary Notes

16. Abstract

A Structurally Integrated Ion Thruster with 8-cm beam diameter (SIT-8) has been developed for attitude control and stationkeeping of synchronous satellites. As optimized, the system demonstrates a thrust $T = 1.14$ mlb (not corrected for beam divergence or double-charged ion content) at a beam voltage $V_B = 1200$ V ($I_{sp} = 2200$ sec), total propellant utilization efficiency $n_u = 59.8\%$ ($n_u \approx 72\%$ without auxiliary pulse-igniter electrode), and electrical efficiency $n_E = 61.9\%$. The thruster incorporates a wire-mesh anode and tantalum cover surfaces to control discharge chamber flake formation and employs an auxiliary pulse-igniter electrode for hollow-cathode ignition.

When the SIT-8 is integrated with the compatible SIT-5 propellant tankage (developed under NASA Contract NAS 3-15483), the system envelope is 35 cm long by 13 cm flange bolt circle with a mass of 9.8 kg including 6.8 kg of mercury propellant. Two thrust vectoring systems which generate beam deflections in two orthogonal directions were also developed under the program and tested with the 8-cm thruster. One system vectors the beam over ± 10 degrees by gimbaling of the entire thruster (not including tankage), while the other system vectors the beam over ± 7 degrees by translating the accel electrode relative to the screen electrode.

17. Key Words (Suggested by Author(s)) Mercury Propellant Electron Bombardment Ion Propulsion System Thrust Vectoring Performance Test 8-cm Diameter	18. Distribution Statement Unclassified - Unlimited	
19. Security Classif. (of this report) Unclassified	20. Security Classif. (of this page) Unclassified	21. No. of Pages 91	22. Price* 3.00

*For sale by the National Technical Information Service, Springfield, Virginia 22151

TABLE OF CONTENTS

LIST OF ILLUSTRATIONS

ABSTRACT

A Structurally Integrated Ion Thruster with 8-cm beam diameter (SIT-8) has been developed for attitude control and station-keeping of synchronous satellites. As optimized, the system demonstrates a thrust T = 5.07 mN (not corrected for beam divergence or double-charged ion content) at a beam voltage V_B = 1200 V (I_{sp} = 2200 s), total propellant utilization efficiency η_u = 59.8% ($\eta_u \approx 72\%$ without auxiliary pulse-igniter electrode), and electrical efficiency η_E = 61.9%. The thruster incorporates a wire-mesh anode and tantalum cover surfaces to control discharge chamber flake formation and employs an auxiliary pulse-igniter electrode for hollow-cathode ignition.

When the SIT-8 is integrated with the compatible SIT-5 propellant tankage (developed under NASA Contract NAS 3-15483), the system envelope is 35 cm long by 13 cm flange bolt circle with a mass of 9.8 kg including 6.8 kg of mercury propellant. Two thrust vectoring systems which generate beam deflections in two orthogonal directions were also developed under the program and tested with the 8-cm thruster. One system vectors the beam over $\pm10^{\circ}$ by gimbaling of the entire thruster (not including tankage), while the other system vectors the beam over $\pm7^{\circ}$ by translating the accel electrode relative to the screen electrode.

SECTION I

INTRODUCTION

The objective of the subject program has been to advance the technology of satellite control ion thrusters to accommodate the demands imposed by spacecraft mission requirements projected for this decade and beyond. This program builds upon the experience gained in development (under NASA Contracts NAS 3-14129 and NAS 3-15483) of a 5-cm Structurally Integrated Ion Thruster (SIT-5) which has been flight qualified for operation at 2.09 mN of thrust. Hughes has extended this technology to include applications where higher thrust levels (one millipound or more) are required. Hughes has also advanced the level of component technology to assure the capability for thruster operation for accumulated beam-on times in excess of 20,000 hours with a capability for 10,000 on-off duty cycles. A dished-grid ion-extraction system has been developed which is capable of remotely controlled misalignment between the screen and accel beam-forming apertures to provide a thrust vector capability in each of two orthogonal directions. A thruster gimbaling system has also been developed to provide an alternative approach to the thrust vector capability. Both beam deflection systems have been designed for a capability of greater than 100,000 deflections.

1

SECTION II

TECHNICAL PROGRAM

The technical program which led to development of the SIT-8 thruster and two thrust vectoring systems is described below.

A.   8-cm THRUSTER DEVELOPMENT

An 8-cm diameter ion-thruster has been developed at Hughes under NASA Contract NAS 3-17791. Design of this prototype thruster was based on a mechanical structure similar to that of the flight-qualified SIT-5 system. Because of this similarity, results of extensive structural and thermal analyses which were successfully implemented under the SIT-5 program are considered to be applicable to this design also. Performance goals of the prototype SIT-8 design were developed in a study by Hudson and Banks[1] and are outlined in Table I. To achieve these goals, design innovations have been incorporated in the discharge chamber and beam-extraction system which were developed or proved under other NASA, Comsat,[2] or Hughes-sponsored programs.

1.   Thruster Description

An isometric drawing of the SIT-8 thruster is shown in Fig. 1. The discharge chamber of the SIT-8 thruster consists of an outer shell assembly, which is formed by rolling thin stainless-steel sheet stock. Structural rigidity of this thin-walled shell is provided by circular stiffening ribs and by flanged sleeves located at the two ends. Axial strength of the structure is provided by the rod-shaped permanent magnets mounted axially around the periphery. Magnets are mounted to the flanges on the ends of the cylinders by lugged collars which are swaged onto the ends of the magnets and spot-welded securely to the

3

TABLE I

SIT-8 Performance Goals

Performance Standards

    Startup to design-performance operation within a minimum time not to exceed 30 min

    Operating characteristics that permit stable closed-loop control operation

    Thrust vector angle, $\pm 10^{\circ}$ in two orthogonal directions

    Projected lifetime, 20,000 hours

    Capability to undergo 100,000 vectoring cycles under space conditions

    Capability to undergo 10,000 restarts under space conditions

    Structurally integrated design

    Thrust, 4.45 mN (5.07 mN uncorrected)

Performance Parameters

    Electrical efficiency, 0.75

    Propellant utilization efficiency 0.85

    Overall efficiency, 0.63

    Ion Formation energy, 280 eV/ion

    Effective Specific impulse, 2944 s

    Net accelerating voltage, 1220 V

    Approximate total weight, 2.1 kg (not including propellant or tankage)

T1245
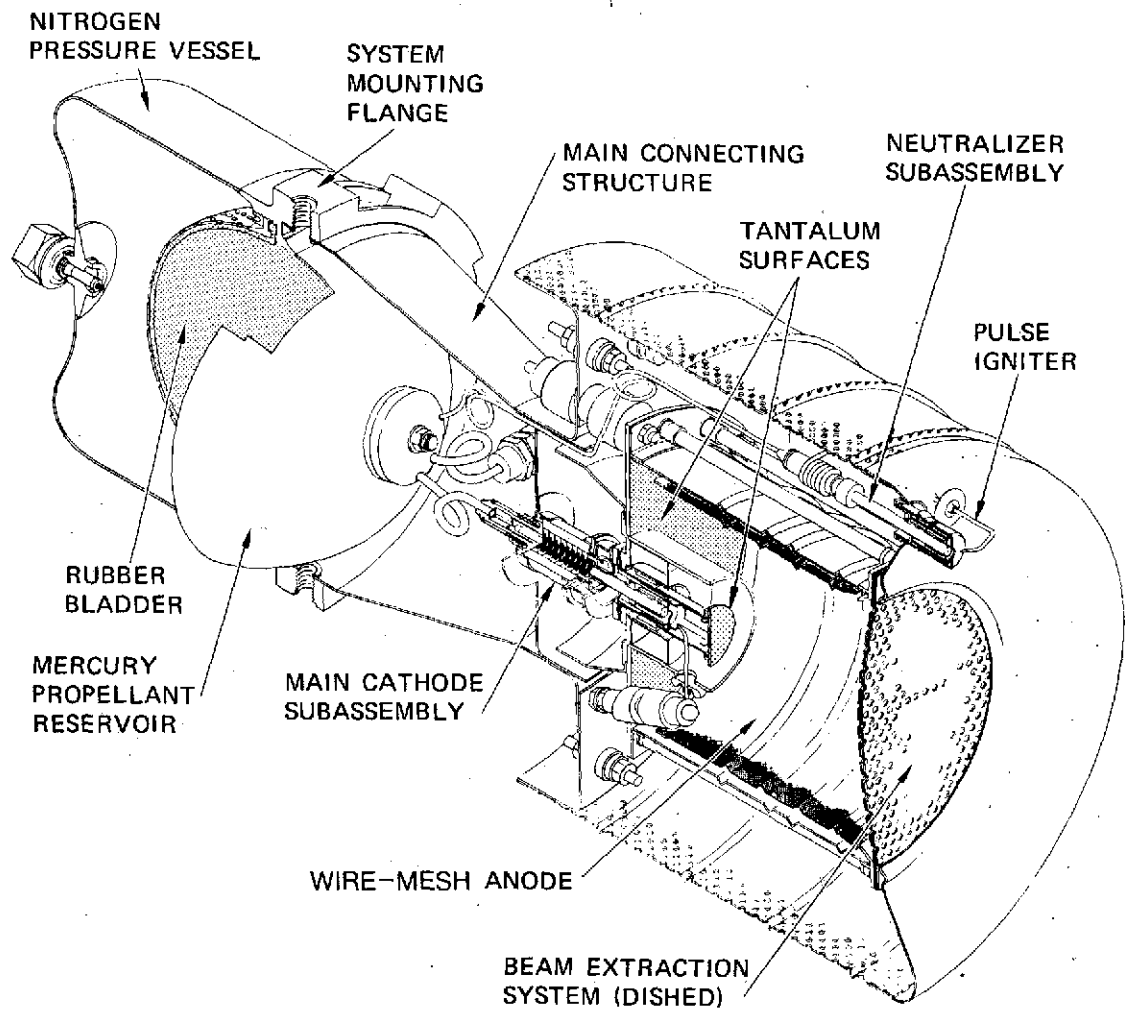
Fig. 1.   SIT-8 ion thruster (with SIT-5 propellant tankage).

flanges. These flanges also serve as the interface between the end-plate on the closed end of the discharge chamber and the mount for the beam-extraction system on the opposite end. An 8-cm cylindrical anode is supported within the shell by means of insulating support posts which are totally shielded against sputtering. As with the thruster shell, stiffening ribs are used to ensure maintenance of its circular cross section.

The Cathode-Isolator-Vaporizer (CIV) assembly located on the upstream end of the 8-cm thruster endplate is essentially the same as that employed successfully with the SIT-5 system. By choosing a vaporizer plug of slightly different shape than that employed in the SIT-5 system, a porous cylinder of the same diameter is capable of supplying the higher mercury vapor flow required for this thruster.

The Neutralizer Isolator Vaporizer (NIV) assembly follows the SIT-5 design closely, with the single modification being the inclusion of a neutralizer isolator. The neutralizer is mounted so that the cathode axis is directed parallel to the axis of the thruster. An enclosed keeper is used, which is mounted directly to the neutralizer-cathode alignment structure. This mounting structure extends the full length of the thruster ground screen and provides a support for all components of the neutralizer assembly. Auxiliary electrodes are employed with both the main and neutralizer cathodes. The electrode tips are located at a distance 0.051 cm axially downstream and 0.051 cm radially outward from the edge of each keeper-electrode aperture, with the neutralizer electrode positioned opposite to the location of the ion beam.

A ring of terminals is provided on the ground screen endplate for the various electrical connections. Connections between these terminals and the thruster components are made using short lengths of uninsulated wire. Sputter shielding is employed at both ends of these terminals to ensure that shorting cannot occur across insulating surfaces.

The SIT-8 beam-extraction system is fabricated with a dish-contoured surface to maintain structural rigidity against deformation, even though the electrode elements are of thin cross section. This permits the use of a high-perveance electrode pair, because the screen-to-accel separation can be set to a small value without fear of electrode shorting under operating conditions where thermal gradients might otherwise cause severe deformation. Critical dimensions of the beam extraction system are listed in Table II.

No propellant tank was designed or fabricated under the subject program, because the SIT-8 thruster was designed for attachment to the existing SIT-5 tankage system. Figure 2 is a photograph of the SIT-8 thruster attached to a propellant tank borrowed from the earlier SIT-5 development.

2. Beam Vectoring System Descriptions

Two beam-vectoring ion-extraction systems have been designed at Hughes under the 8-cm thruster development program. Both of these systems were designed to be capable of achieving the design goal of providing ion-beam thrust vectoring of $\pm 10^{\circ}$ in two orthogonal directions. Both systems employ the SIT-8 extraction-electrode aperture pattern described in Table II. One of the systems, the Dished Grid Vector System, employs a stepping motor-driven cam-drive actuator to displace the accel electrode relative to the screen electrode in either of two orthogonal directions. As shown in Fig. 3, the accel grid is supported by flexure-column supports which are predeflected to keep the grid in contact with the cam actuator. To provide the thermal stability necessary to satisfy the design goal for pointing accuracy $(\pm 0.1^{\circ})$, a nickel-iron alloy has been chosen for fabrication of the screen-and-collar polepiece. This alloy has a coefficient of thermal expansion that matches that of the molybdenum extraction electrodes. The second system developed under the on-going effort is a Thruster Gimbaling System which achieves thrust vectoring by gimbaling the

TABLE II

Dimensions of the SIT-8 Beam Extraction System

Dimension / Grid Element	Optical Transparency, %	Grid Thickness, mm	Aperture Diameter, mm	Center-to-Center Spacing, mm	Electrode Separation, mm	Dish Radius of Curvature, cm	Number of Apertures
Screen	67.5	0.406	1.905	2.209	0.635	30.00	1270
Accel	47.6	0.508	1.600				

T1264

8

M10275

Fig. 2.   8 cm structurally integrated ion thruster (SIT-8).

VOLTAGE
ISOLATOR

B-B FLEXURE
COLUMN
SUSPENSION

B

B

A

A

A-A CAM
ACTUATOR

ACCEL
ELECTRODE
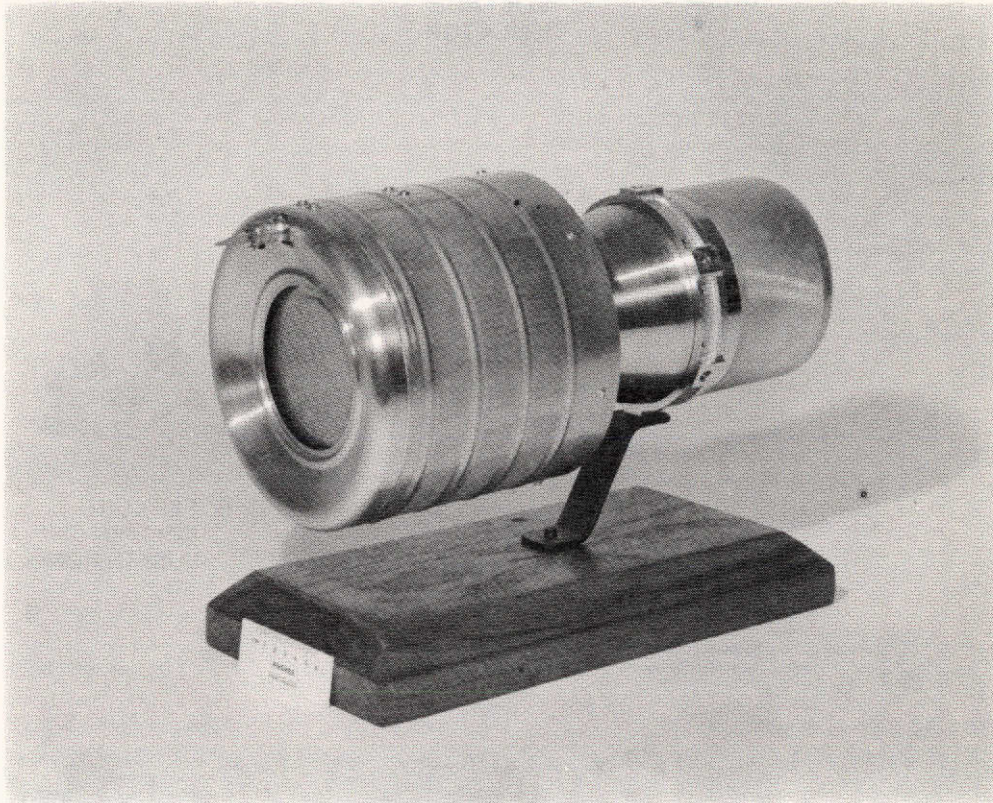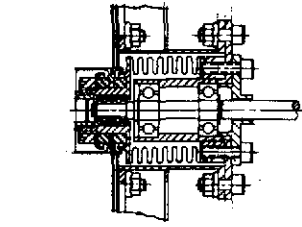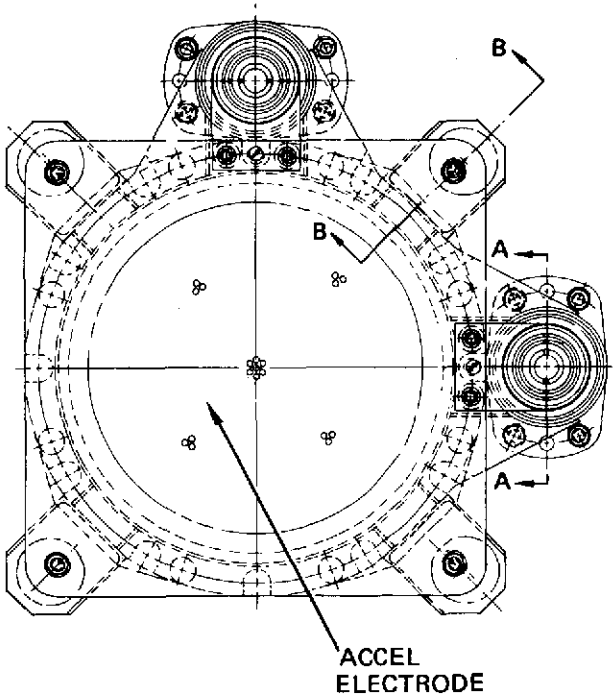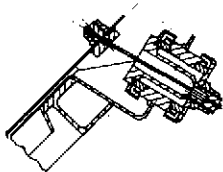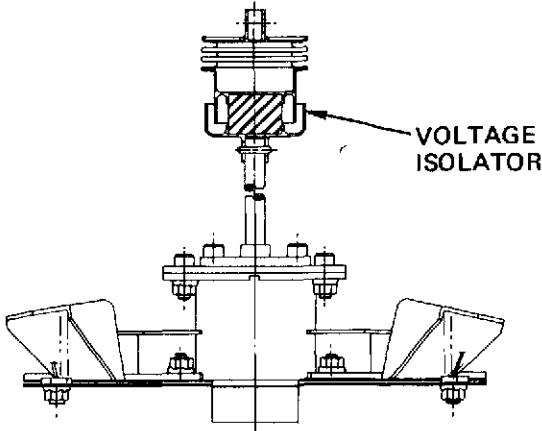
Fig. 3.   Dished grid vectoring system (DGVS).

entire thruster (not including propellant tankage) about either of two orthogonal axes. As shown in Fig. 4, two linear actuators are used to tilt the thruster about the two orthogonal axes of the gimbaling system. In both systems, end-of-travel stops are employed and actuator position is determined by counting the number of motor steps from the end-stop location.

3. System Performance

The capabilities of the SIT-8 thruster system are thought to conform closely to the performance goals listed in Table I, except that electrical and propellant efficiency has fallen short of their projected values by virtue of design compromises discussed at length in Section II-B. Typical discharge-chamber performance characteristics for SIT-8 thruster operation are listed in Table III. The tradeoff between propellant utilization efficiency η_u and ion generation energy ϵ_I is shown by the curve in Fig. 5 marked "igniter." Other curves also shown in Fig. 5 indicate the magnitude of performance improvements which can be achieved by removal of design constraints imposed on the SIT-8 design for reasons other than the advancement of discharge-chamber performance.

B. THRUSTER OPTIMIZATION

In the following discussion, criteria are developed to evaluate discharge-chamber performance of the SIT-8 thruster configuration and to compare this performance to the performance goals listed in Table I. Techniques of discharge-chamber optimization are discussed and the use of a reduced-transparency beam extraction system at high discharge-chamber power is identified as a means of achieving increased efficiency. Experimental evidence is presented to substantiate this overall system conclusion, which is consistent with

3166—40 R1

LINEAR ACTUATORS

MoS$_2$ LUBRICATED BEARING

THRUSTER MOUNTING RING

SPACECRAFT MOUNTING FLANGE
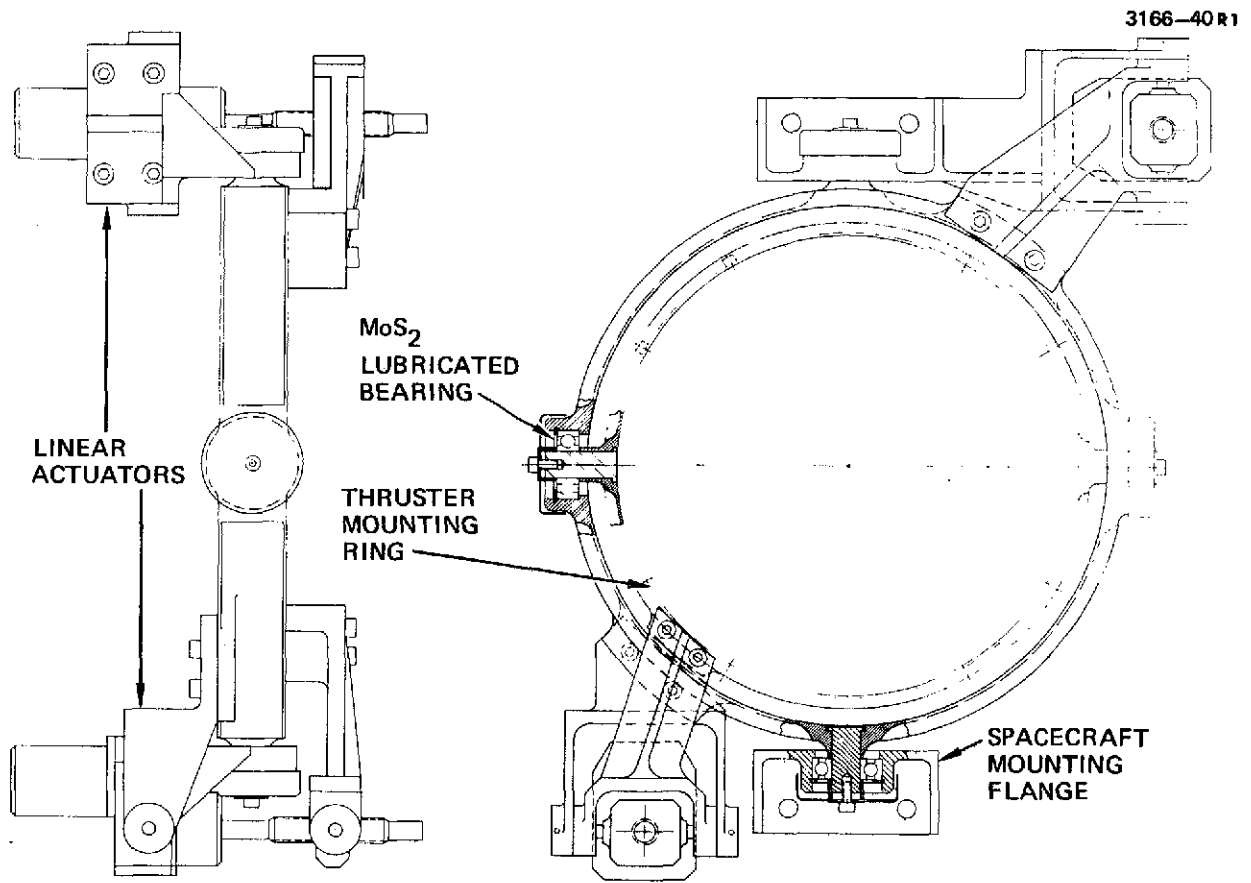
Fig. 4.   Thruster gimbaling system.
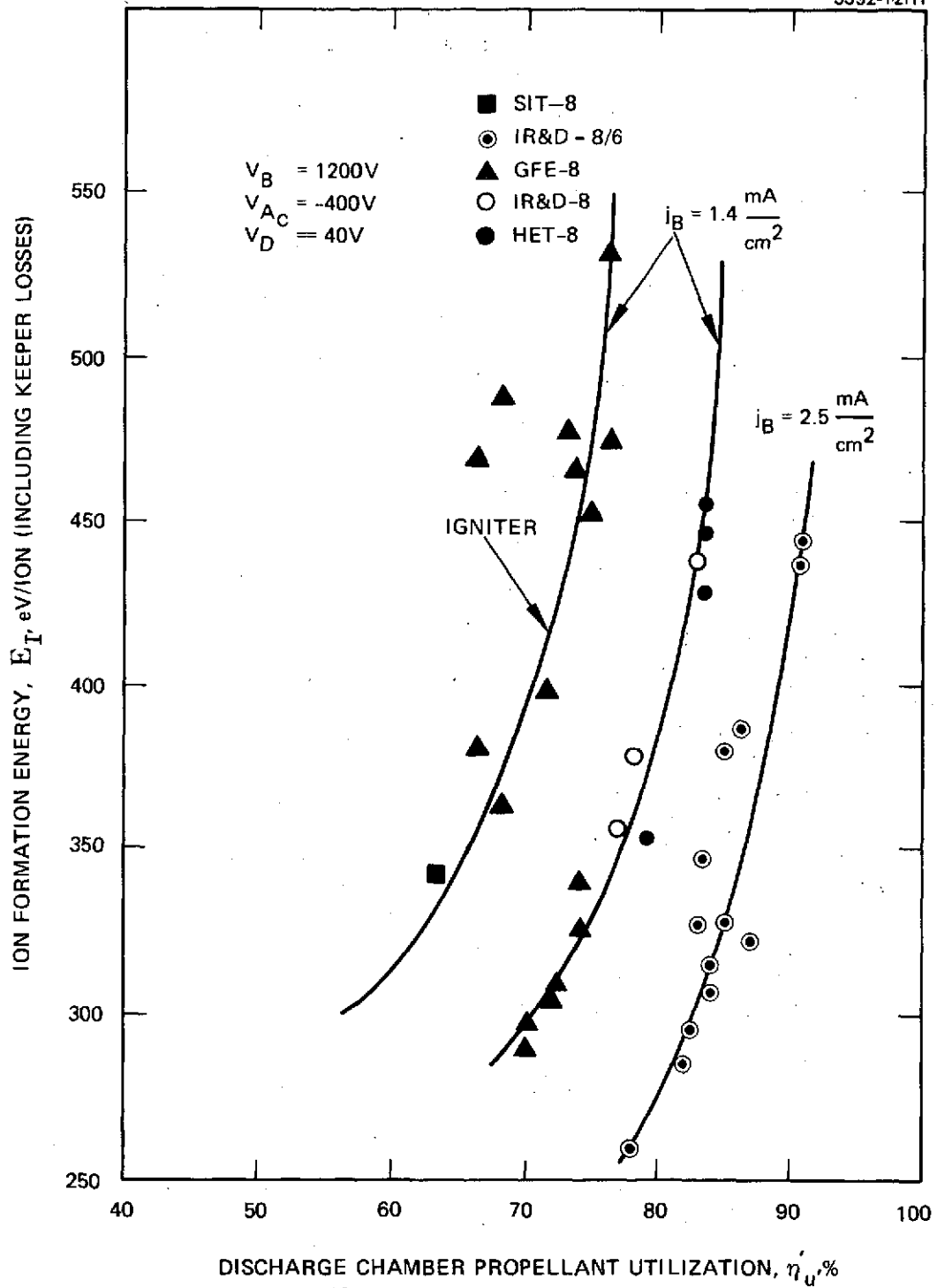
Fig. 5. Thruster performance comparison. (Some points have been scaled to compensate for varying beam currents.)

TABLE III

SIT-8 Thruster Performance Summary
(auxiliary igniters installed)

Thrust[a] (ideal), mN	5.07	
Specific impulse,[a] s	2072	
Total input power, W	143.10	
Total efficiency,[a] %	37.0	
Power efficiency, %	61.9	
Total utilization,[a] %	59.3	
Discharge utilization,[a] %	62.9	
Total neutral flow, mA	120.7	
Power/thrust,[a] W/mN	28.24	
eV/ion excluding keeper, V	294	
eV/ion including keeper, V	344	
Beam current, I_B, mA	72.2	
Beam voltage, V_B, V	1200	
Neutralizer coupling potential, V_c, V	-20	
Output beam power, W		88.08
Accelerator voltage, V_{Ac}, V	-300	
Accelerator drain current, I_{Ac}, mA	0.30	
Accelerator drain power, W		0.37
Discharge voltage, V_D, V	40	
Neutralizer coupling, I_c, A	0.53	
Discharge power, W		21.2
Cathode		
Keeper voltage, V_{MK}, V	14.6	
Keeper current, I_{MK}, A	0.250	
Keeper power, W		3.63
Heater voltage, V_{MCH}, V	5.5	
Heater current, I_{MCH}, A	2.5	
Heater power, W		13.75
Vaporizer voltage, V_{MV}, V	2.1	
Vaporizer current, I_{MV}, A	0.8	
Vaporizer power, W		1.68
Flowrate, mA	114.7	
Neutralizer[b]		
Keeper voltage, V_{NK}, V	16.0	
Keeper current, I_{NK}, A	0.700	
Keeper power, W		11.2
Heater voltage, V_{NCH}, V	0	
Heater current, I_{NCH}, A	0	
Heater power, W		0
Vaporizer voltage, V_{NV}, V	3.5	
Vaporizer current, I_{NV}, A	0.5	
Vaporizer power, W		1.75
Flowrate, mA	7.0	
Neutralizer coupling power, W		1.44

[a] Accounting for neutralizer floating potential but neglecting beam divergence and double ionization.

[b] The neutralizer was not operated during this test, the values given here are nominal for foil-insert cathode operation.

T1355

Kaufman's thesis result, [3] that, for a given discharge-chamber geometry, the neutral particle losses are proportional to the transmittance of the beam extraction system, since the neutral particle density is a constant of the system. Finally, the need is established to control metal-flake formation within the discharge chamber, and a number of techniques are introduced which are expected to entirely eliminate this potential problem area.

1.   Performance Capabilities

In continuing 8-cm thruster development, numerous configurations of the basic Hughes design have been explored which differ by discrete changes in discharge-chamber configuration and in the critical dimensions of the beam-extraction system. [4]   Only one configuration has demonstrated performance that is consistent with the goals set forth in Table I. This configuration employed a reduced-transparency beam-extraction system. The clear superiority of this configuration over alternative designs (including all configurations explored under the subject contract is demonstrated in the following discussion.

To compare experimental data which are taken from more than one discharge-chamber configuration and calculated for numerous setpoints, it is essential that the comparison be made in a general context to avoid piecemeal comparisons between two alternative configurations where one parameter looks better and one looks worse. The most general parameter for evaluation of thruster performance as a whole is the total efficiency η_T which is equal to the electrical efficiency η_E multiplied by the propellant-utilization efficiency η_u. For comparison of discharge-chamber configuration only, a more pertinent parameter is the discharge-chamber total efficiency η_T' which is the product of the discharge-chamber electrical efficiency η_E' multiplied by the discharge-chamber propellant utilization efficiency η_u' as defined below,

15

$$\eta'_T = \frac{P_B}{P_B + P_D} \eta'_u \, ,\tag{1}$$

where P_B = beam power and P_D = discharge power.

Equation (1) can be related more directly to program objectives through the goal requirements for thrust and specific impulse. In keeping with the restrictions of eq. (1), a discharge-chamber effective specific impulse (reduced specific impulse) $I'_{sp, eff}$ is defined below:

$$I'_{sp, eff} = 99.7 \, \eta'_u \, V_N^{1/2} \, ,\tag{2}$$

where V_N is the net accelerating voltage and is equal to the beam voltage V_B plus the discharge voltage V_D. Also, the maximum thrust T which is generated by a beam current I_B is

$$T = 2.047 \times 10^{-3} \, I_B \, V_N^{1/2} \, mN \, .\tag{3}$$

By requiring $T = 4.07 \times 10^{-3}$ mN (1.14 mlb) in accordance with program goals, and combining eqs. (2) and (3), $I'_{sp,eff}$ can be written as the reduced power P'_T.

$$I'_{sp, eff} = 40.25 \, \eta'_u \, P'_T \, sec\tag{4}$$

where $P'_T = V_N I_B = (V_B + V_D) I_B$. Now, recalling the definition of η'_T from eq. (1), eq. (4) can be rewritten as shown below:

$$I'_{sp, eff} = 40.25 \, \eta'_T (P_B + P_D) \, sec \, .\tag{5}$$

Using $(P_B + P_D)$ as a variable, curves can be obtained which express the efficiency of the discharge chamber and the beam extraction system for conversion of power into thrust at a given specific impulse. No significant loss in generality is introduced by omitting the "fixed" losses from this analysis. These losses are not neglected but merely set aside for separate consideration. The discharge-chamber-related parameters employed in this analysis are related to contract objective by noting the numerical relationship shown in Table IV.

In Fig. 6, the reduced specific impulse $I'_{sp, eff}$ is plotted against the reduced power P'_T with curves of constant η'_T indicated. Thruster operating data are superimposed on this display, which represent the results of several configurational variations of the SIT-8 thruster carried out in the current NASA-funded optimization and from previous operation of an early laboratory-type 8-cm thruster (LAB-8), and a current flight-type 8-cm thruster (HET-8) developed under a Hughes IR&D Program.

The data presented in Fig. 6 are found to cluster in two distinct groups — one group for operation with the nominal 8-cm beam diameter and a second group for thruster operation in which a beam mask was employed upstream of the screen electrode to reduce the active beam transmission diameter to $D_B = 6$ cm. Separate curves are drawn through the two groups. These curves represent a mapping of the more conventional performance curves into the parameter space of Fig. 6. (The lower curve, for instance, is a mapping of the intermediate curve of Fig. 5.) It is clear that data corresponding to the restricted beam diameter form a superior set with respect to contract goals. These data exhibit a maximum reduced efficiency $\eta'_T = 67\%$ for operation with a discharge-chamber energy $\epsilon_I = 330$ eV/ion. A summary of parameter values for this most efficient of the test points is given in Table V. The fact that superior performance is achieved with a reduced number of apertures is not unexpected and is explained fully in the following section which deals with discharge-chamber optimization.

17
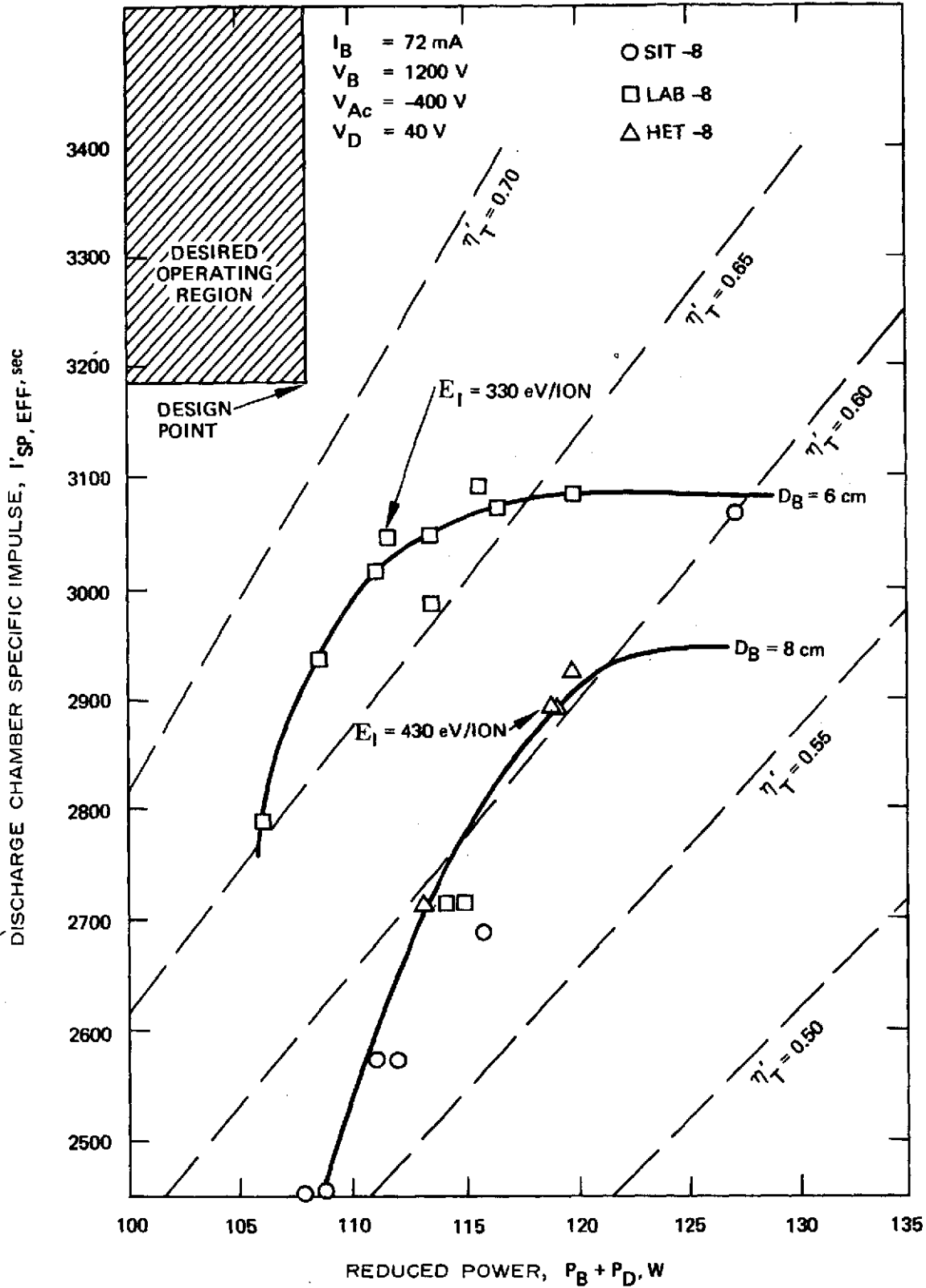
Fig. 6. Global plot showing 8-cm thruster efficiency, η_T' for beam diameters D_B = 8 cm and D_B = 6 cm.

18

TABLE IV

Contract Design Objectives (Numerical estimates based on the contract
goals shown in Table I)

Beam power

$$P_B = 1220 \text{ V} \times 0.072 \text{ A} = 87.8 \text{ W}$$

Discharge power

$$P_D = 280 \text{ eV/ion} \times 0.072 \text{ A} = 20.2 \text{ W}$$

Reduced power

$$P_T' = P_B + P_D = 108 \text{ W}$$

Total propellant flowrate

$$I_{Hg} = 0.072 \text{A}/0.85 = 0.0848 \text{ A}$$

Neutralizer flowrate

$$I_{N, Hg} = 0.0060 \text{ A}$$

Discharge-chamber flowrate,

$$I_{M, Hg} = I_{Hg} - I_{N, Hg} = 0.0788 \text{ A}$$

Discharge-chamber propellant utilization

$$\eta_u' = 0.072/0.0788 = 0.913$$

Reduced specific impulse,

$$I_{sp, eff}' = 99.7 \times 0.913 \ (1220)^{1/2} = 3180 \text{ sec}$$

---

[a]The value $I_{N, Hg}$ = 6 mA has been selected as the mini-
mum value consistent with the requirement for 20,000
hours of neutralizer operating lifetime based on results
reported at the NASA Lewis Research Center.[5] (See
Section II-B-5).

T124

19

TABLE V

Lab-8 Thruster Performance Summary (6 cm beam aperture)

Thrust[a] (ideal), mN	5.07	
Specific impulse, [a] sec	2819	
Total input power, W	128.3	
Total efficiency, [a] %	54.9	
Power efficiency, %	68.1	
Total utilization, [a] %	80.7	
Discharge utilization, [a] %	86.5	
Total neutral flow, mA	89.2	
Power/thrust, [a] W/mN	25.31	
eV/ion excluding keeper, V	294	
eV/ion including keeper, V	326	
Beam current, I_B, mA	72	
Beam voltage, V_B, V	1200	
Neutralizer coupling potential, V_c, V	-20	
Output beam power, W		86.4
Accelerator voltage, V_c, V	-1000	
Accelerator drain current, I_{Ac}, mA	0.24	
Accelerator drain power, W		0.24
Discharge voltage, V_D, V	40	
Neutralizer coupling current, I_c, A	0.53	
Discharge power, W		21.2
Cathode:		
Keeper voltage, V_{MK}, V	9.7	
Keeper current, I_{MK}, A	0.235	
Keeper power, W		2.28
Heater voltage, V_{MCH}, V	0	
Heater current, I_{MCH}, A	0	
Heater power, W		0
Vaporizer voltage, V_{MV}, V	3.8	
Vaporizer current, I_{MV}, A	1.0	
Vaporizer power, W		3.8
Flow rate, mA	83.2	
Neutralizer:		
Keeper voltage, V_{NK}, V	16.0	
Keeper current, I_{NK}, A	0.700	
Keeper power, W		11.2
Heater voltage, V_{NCH}, V	0	
Heater current, I_{NCH}, A	0	
Heater power, W		0
Vaporizer voltage, V_{NV}, V	3.5	
Vaporizer current, I_{NV}, A	0.5	
Vaporizer power, W		1.75
Flow rate, mA	6.0	
Neutralizer coupling power, W		1.44

[a]Accounting for neutralizer floating potential but neglecting beam divergence and double ionization.

T 1248

20

Before concluding the discussion of performance capabilities, it is necessary to note that the goals of the subject contract effort $(I_B = 72 \text{ mA}, \eta_I = 280 \text{ eV/ion}, \text{ and } \eta_E = 0.75)$ imply a value for "fixed" losses of only 9.1 W. While this power level might be achieved, it seems quite low on the basis of thruster operating experience at Hughes. Based on the more typical set of minimum "fixed" losses given in Table VI, a specified goal of $\eta_E = 0.73$ is projected.

TABLE VI

Minimum Anticipated "Fixed" Power Losses

Cathode tip heaters[a]	0.0 W
Main vaporizer	3.0 W
Neutralizer vaporizer	1.25 W
Neutralizer keeper	7.50 W
	11.75 W

[a]Experience has shown that thruster operation with zero power to cathode tip heaters may only be realizable when tantalum foil inserts coated with R-500 (or equivalent) are used (see Section II-B-4).

T1249

2. Discharge Chamber Optimization

Optimization of the 8-cm discharge chamber has centered on determination of optimal geometrical relationships: baffle size, diversion-port transparency, anode length and location, and level of current to the magnetic baffle[6] (including the final zero-current configuration) and keeper electrode.

a. Magnetic Baffle

An active magnetic baffle was incorporated originally into the 8-cm discharge-chamber design as a variable parameter to aid in optimization and to permit efficient operation over a range of setpoints without the need for geometrical changes. In Table I, however, only one efficient setpoint is required, and so the possibility arose of eliminating the active magnetic baffle (in favor of an inactive baffle) as a means to decreasing the number of active elements in the thruster system.* This possibility has been pursued under the current 8-cm thruster development.

It has almost universally been found that increasing magnetic-baffle current produces increasingly better performance until a point is reached at which a relaxation oscillation is set up in the discharge chamber. This oscillation is similar to one which is produced when an inactive baffle of too large a diameter is used; the oscillation evidently results from too large an impedance between the main discharge plasma and keeper plasma. A study was carried out to ascertain the effects on the magnetic field geometry of the magnetic baffle at various current levels, and of several alternative baffling systems. The results of this study indicated that the effects of the active magnetic baffle are threefold: First, the baffle increases the impedance of the gap between the plasma in the cathode-cup polepiece region and main

---

*This involves elimination of the baffle solenoid coil only. No separate power supply is required for the active magnetic baffle which can be activated by running discharge current through the coil.

22

discharge plasma in much the same fashion as an inactive baffle. Second, the use of the baffle more evenly distributes magnetic-field lines over the region of the screen; this is likely to produce a more uniform density of primary electrons. Third, the baffle produces a region of low (or zero) magnetic field in the cathode-keeper region.

In the final SIT-8 design, an inactive baffle fabricated of nonmagnetic material has been employed and the resulting thruster performance evaluated; the stability of this configuration is excellent, and performance is close to that achieved with the active magnetic baffle.

b.   Low Transparency Optics

Experiments with beam-aperture-limiting masks have demonstrated that reducing the open area of the extraction electrode reduces neutral losses and thus improves discharge-chamber performance. At present, it is believed that the optimal open area is approximately that which corresponds to the open area which is achieved by operating with the SIT-8 beam extraction system, but restricting the beam diameter to D_B = 6 cm (see Fig. 6).[*] Data for operation in this configuration are given by the curve shown in Fig. 5 representing most efficient operating performance.

c.   Pulse Ignition

Experience with pulse-ignition of the hollow cathode has shown that the inclusion of an auxiliary igniter electrode can produce discharge-chamber instabilities and seriously degrade thruster performance. Figure 5 presents a summary of the thruster

----

[*]Alternative approaches have been identified elsewhere. In a Hughes IR&D program operation with low transparency grids at D_B = 8 cm has yielded performance similar to reduced beam-diameter operation. At NASA LeRC, Banks and Hudson report high efficiency operation with the SIT-8 hole pattern in the screen electrode, but with the optical transparency of the accel electrode reduced to a value of less than 20% open.

performance of three similar 8-cm thrusters. The most consistent feature of points located on the curve of poorest performance is the presence of auxiliary-pulse-igniter electrode; experiments indicate that it is the protrusion of the igniter into the plasma inside the cathode-cup pole-piece that produces the degradation. From the measurements described above, it is now known that discharge-chamber stability is highly sensitive to the geometry of this region. It seems likely that the discharge would be less sensitive to the presence of the igniter electrode if a totally field-free region were established inside the cathode cup pole-piece; this possibility should be investigated in any future study. Independent of the results of this investigation, however, the more direct means of dealing with the problem of igniter-electrode perturbations might be to eliminate the auxiliary electrode altogether applying high-voltage pulses directly to the keeper electrode. The pulse-to-keeper method of ignition has been demonstrated by Wintucky,[7] and has been shown to be equally effective as the pulse-to-auxiliary electrode method.

3.   Metal Flake Control

The motivating cause for termination of the 9700 hour life test of the SIT-5 thruster system (at LeRC) was the presence of a metal flake which fell over one of the beam-forming apertures of the screen electrode and disturbed the beam trajectory, causing it to impinge directly on elements of the electrostatic thrust-vectoring accel electrode.[5] Direct impingement of a large part of the beamlet current quickly severed an accel element and caused it to fall into a position where a short circuit was established between the screen and accel electrode, making further beam extraction impossible. John Power[8] of LeRC has shown that the flakes form inside of the discharge chamber as a result of ion-bombardment sputtering of cathode-potential surfaces and that essentially all of the sputtered material is ultimately deposited on the anode from which it eventually flakes off. His studies have shown that the sputter-deposited film exhibits good adherence with the anode surface up to the point where film deposits are accumulated which are sufficiently thick to result in separation of the interstitial layers at which time spalling and flake formation begin to occur.

24

Metal flake control techniques were tested in the SIT-8 thruster under the contract effort. The techniques had earlier been developed at LeRC to prevent interruption of thruster operation by metal flake perturbations.[8] These techniques, listed below, concentrate on each stage of the problem from the ion-bombardment sputtering process, to the adherence of anode films, and to the neutralization of the metal flakes.

- Reduce discharge voltage and doubly charged-ion concentration to minimize ion-bombardment sputtering

- Employ cover surfaces to reduce the ion-sputtering yield

- Employ a wire-mesh anode to prevent large-flake detachment

In the discussion which follows, each of these techniques is described briefly.

a.   Reduce Discharge Voltage

One approach toward overcoming the anode-coating problem is to substantially lower the sputtering yield from cathode-potential surfaces by lowering the discharge voltage from values near 40 V to values nearer to 35 V. The SIT-8 thruster discharge can readily be made to operate at lower discharge voltages by any of a number of possible techniques, but usually with some loss in discharge-chamber propellant utilization efficiency. Modifications which have been found to lead toward this goal are listed below:

- Increasing the gap between the electron baffle and the lip of the cathode polepiece

- Decreasing the transparency of propellant-diversion ports (when employed) in the cathode polepiece

- Decreasing the active magnetic-baffle current (when employed)

25

- Increasing the radial divergence of the magnetic field as by extending the collar polepiece

- Lengthening the discharge chamber.

Reduction in discharge voltage is expected to have the twofold benefit of reducing the ion-bombardment energy and simultaneously reducing the fraction of doubly charged mercury ions; the doubly charged ions have been identified as being responsible for most of the sputtering,[8] because they bombard the cathode-potential surfaces with twice the energy of singly charged ions.

b. Cover Surfaces

The goal of reducing the rate of ion-bombardment erosion of cathode-potential surfaces by discharge voltage reduction can be supplemented in a significant fashion by selecting materials with high sputtering threshold and low sputtering yield. In a study of cathode sputtering of metals by slow mercury ions, Askerov and Sena[9] have shown that, of all the metals studied, tantalum appears to exhibit the highest threshold energy (~35 eV) below which essentially no ion bombardment sputtering occurs. Also, Wehner[10] has shown that tantalum exhibits a relatively low sputtering yield in the range of interest for this application (i.e., from 35 eV to 80 eV of ion energy). On the basis of these results, the electron baffle and a cover sheet placed over the iron endplate of the SIT-8 thruster have both been fabricated of tantalum.

c. Wire Mesh Anode

As a means for controlling metal flake formation, Banks has suggested fabrication of the anode from fine mesh screen material.[8] Such an anode would be expected to develop a coating varying substantially in thickness over each mesh unit and correspondingly varying in adhesion to the substrate with the thinner portions of the substate adhering well and the thicker portions adhering poorly as shown in Fig. 7. With such a variation in coating adhesion

SPUTTERED FLUX FROM
DISCHARGE CHAMBER COMPONENTS

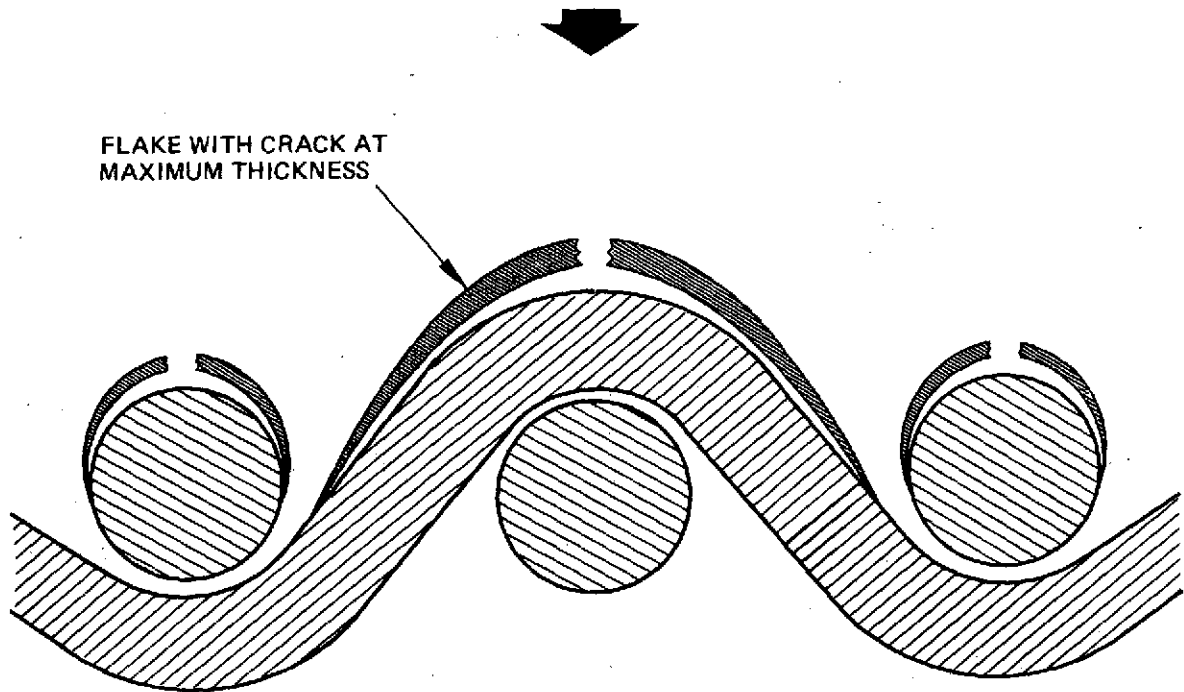FLAKE WITH CRACK AT
MAXIMUM THICKNESS

Fig. 7. Use of wire mesh anode to control metal flake
formation.

over each mesh unit, it is anticipated that the unit flakes would remain attached to the mesh almost indefinitely by their adherent segments; if an when they do detach, no flakes larger than the mesh dimension would be expected to fall off. If the mesh dimension is made sufficiently small, therefore, the spalled flakes would create none of the severe problems caused by the centimeter-size flakes which spalled from the anode near the end of the 9700-hour endurance test and which led to the termination of that test.

A screen mesh anode has been fabricated for use with the SIT-8 thruster currently under development. To achieve suitably small mesh dimension, the same mesh material was used as is employed in fabrication of the Hughes high-voltage isolators. The resulting anode does not possess the same degree of structural rigidity exhibited by solid anode cylinders used in previous thruster developments and may not be able to survive the booster-launch environment. If further analysis confirms this deficiency, the anode can be provided with the necessary rigidity by attachment to a steel tube which will surround it.

4. Cathode Design

In 8-cm thruster development, a new cathode concept has been developed by the Lewis Research Center[11] in which the tantalum-foil insert has been replaced by a porous-tungsten plug impregnated with a mixture of 4 parts BaO to 1 part CaO and 1 part Al_2O_3. This replacement was motivated[11] for the same reasons that impregnated (Phillips-Type) cathodes receive overwhelming acceptance for use as high-current electron emitters for use in modern high performance electron-beam devices; with the porous insert, a greater quantity of emissive material can be stored in a manner which makes it readily accessible to replenish emissive material which is removed from active surfaces by evaporation or ion bombardment. Furthermore, the porous tungsten is less prone than tantalum foil to chemical

28

combination with emissive material which serves to deplete the supply. In conformance with instructions of the NASA Project Manager, cathodes with porous inserts have been used exclusively under the subject contract. In operation of the SIT-8 thruster, porous tungsten inserts have consistently required higher heater power to achieve ignition than have their foil-insert counterparts. Under the subject program, the cathode was ignited by applying 800 V to the keeper electrode, flowing mercury through the cathode at or above its nominal value for thruster operation, and heating the cathode tip. Ignition was achieved only after 50 W of heater power was applied to the cathode tip, and subsequent re-ignition required the same amount of power. This heater requirement compares poorly with the lower requirements of similar cathodes with foil inserts which require a 32 W for first ignition and after conditioning can be re-ignited reliably with 18 W of heater power.[12] Other disadvantages of cathode with impregnated inserts are apparent during operation after ignition is achieved. With the SIT-8 thruster, 5 W to 10 W heater power must be maintained on the cathode tips after ignition to avoid excessively high (>20 V) keeper voltages at both the main and neutralizer cathodes. That this was the result of employing the porous inserts was made dramatically clear by the ease of ignition and drop in keeper operating potential after a small amount of Baker R-500 emissive material was painted directly on the cathode tip of an early model configuration. This improvement continued in subsequent operations when no additional material was painted on.

The need to maintain cathode heat after ignition when porous-tungsten impregnated materials are used is further substantiated by recent experimental measurements with an alternative cathode design presently being investigated under a Hughes IR&D Program. As shown in Fig. 8, this cathode is constructed in a flight-type package which is totally compatible with the current 8-cm thermal and mechanical design. It is currently being fabricated under Hughes IR&D program and has not
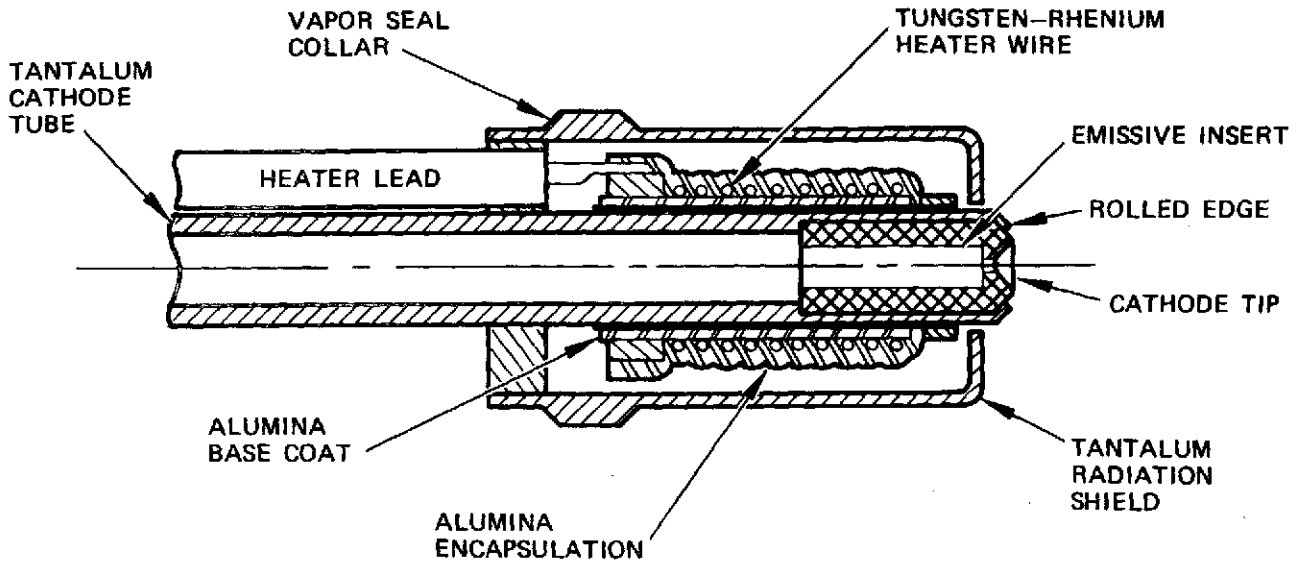
Fig. 8. Hughes porous-tungsten-tip cathode subassembly.

yet been tested with the flame-spray heater. Preliminary results have been achieved, however, using a pressed-on tantalum-sheath heater of the type used early in the SIT-5 thruster development.[13] Under these conditions, ignition is achieved consistently with less than 25 W of power with an open-circuit keeper voltage of +200 V and a mercury flow-rate near to the nominal value for neutralizer operation. In general, operation of this cathode compares closely with similar cathodes having foil inserts, except that cathode tip power was required to maintain the keeper voltage in the normal operating range for neutralizer operation even after many hours of operation, whereas no tip power is required with cathodes having foil inserts; the dependence of keepr voltage on tip power is shown in Fig. 9 for the cathode with the porous-tungsten tip.

5.   Neutralizer Flowrate

In the 9700 hour test of a SIT-5 thruster at the Lewis Research Center, Nakanishi and Finke[5] have observed that the main-cathode keeper voltage was measured within a range of 12 to 15 V throughout the test and that no heater power was required except during startups. No evidence was found to indicate any degradation of main cathode performance as a result of the 9700 hour operation. The neutralizer keeper voltage and floating potential, on the other hand, gradually rose with time, but could be compensated for by increasing tip heater power. In post-test inspection, it was discovered that erosion occurred at the aperture of the chamfered surface of the neutralizer cathode tip to the extent that the flow orifice was enlarged to more than double its original diameter. Preliminary data taken by Weigand[5] have indicated that the neutralizer-tip erosion can be a strong function of neutralizer flowrate. Weigand's data have indicated that for hollow cathode flowrates at or above $I_{N, Hg}$ = 6.9 mA, the tip-erosion rate is reduced by over two orders of magnitude from the rate evidenced in the SIT-5 test where the flowrate was 1.7 mA < $I_{N, Hg}$ < 2.5 mA. This reduction was observed even for cathodes operating without any
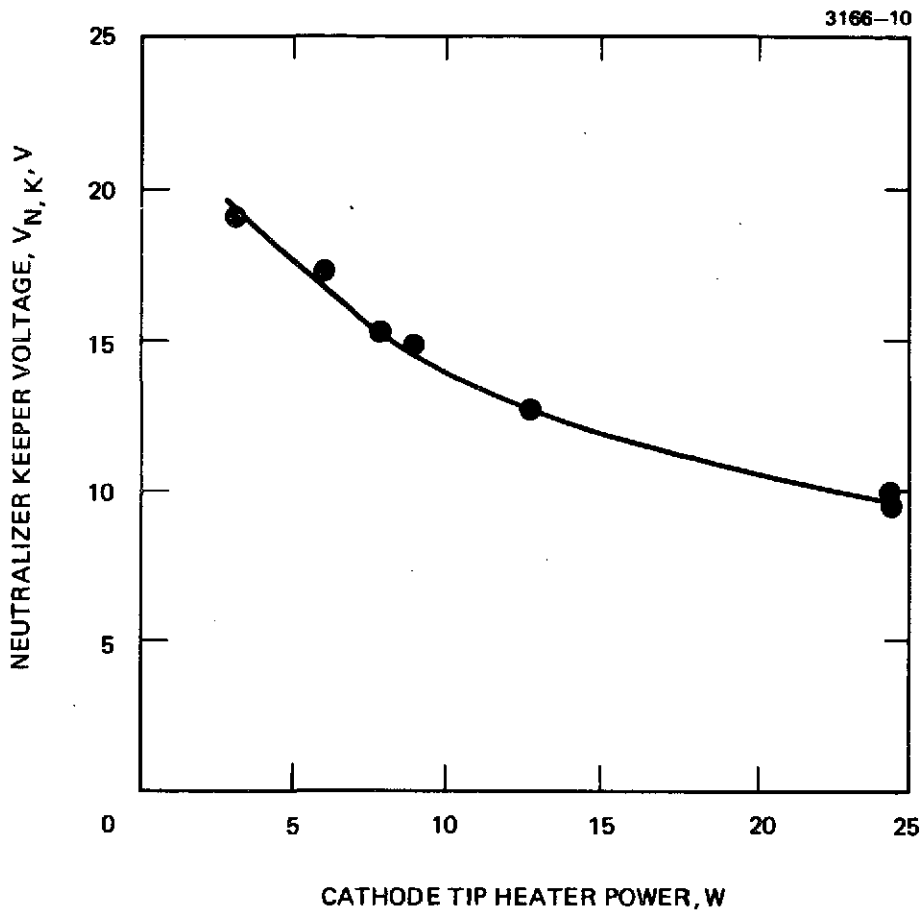
Fig. 9.   Impregnated tip heater operation.

inserts or emissive coatings. On the basis of these observations, in all SIT-8 thruster operation has been conducted at slightly higher neutralizer flowrates ($I_{N, Hg} \gtrsim 6$ mA) than those which obtained in SIT-5 thruster operation to prevent excessive neutralizer-tip erosion.

C.   VECTORING SYSTEM DEVELOPMENT

Two beam vectoring systems have been designed under the subject contract. One system, the Dished Grid Vectoring System, (DGVS) employs a stepping-motor cam-drive actuator to displace the accel electrode relative to the screen electrode in either of two orthogonal directions. The accel grid is supported by flexure-column supports which are predeflected to keep the grid in contact with the cam actuator. The second system, the Thruster Gimbaling System (TGS), achieves thrust vectoring by gimbaling the entire thruster (not including propellant tankage) about either of two orthogonal axes. Two linear actuators are used to tilt the thruster about the two orthogonal axes of the gimbaling system. End-of-travel stops are employed with both systems, and angular position is determined by counting the number of motor steps from the end-stop location.

1.   Design Analysis

In the design analysis which preceded development of the vectoring system numerous tradeoffs were considered in selection of suspension and actuator options particularly for providing force and displacement to move the electrodes for the DGVS. Electromechanical devices offered the best response times, while thermal devices offered higher forces, but poor response times. Mechanical devices were limited in the types of motion permitted, because of possible detrimental effects to moving parts in the high-temperature hard-vacuum spacecraft environment. Chips and flakes of sputtered

material from thruster operation were recognized as an additional hazard to close-clearance mechanical devices. Actuators with very small displacements (less than 0.001 cm) were avoided since they would require high-ratio transmission devices resulting in high loads, reduced reliability, increased sensitivity to dimensional tolerance and temperature variations.

For design of the DGVS, three essential elements were analyzed: the actuator, the electrode suspension, and the transmission which joins the former two elements. In this study, it was assumed uniformly that each system must be capable of exerting the maximum deflection ($\sim$0.051 cm) and force ($\sim$4.4 N) that might be required to accommodate the largest electrode apertures and the thickest electrodes that might be used.

a.   Suspension System

The DGVS utilizes the misalignment of two dished electrodes to vector the thrust. This is accomplished by fixing one electrode and moving the other. Since the electrodes are spherically dished and a uniform separation must be maintained between electrodes, the moving electrode must roll about the fixed electrode. Techniques for approximating this motion are described in the discussion which follows.

(1)   Kinematics — For small deflections, the rolling motion can be approximated by end-pivoted rigid support links, which are positioned initially so that the pivots lie on a radius from the center of curvature of the electrode dish, as shown in Fig. 10. A two-dimensional diagram of a single support is shown in Fig. 11. From this diagram the electrode displacement, S, is seen to be

$$S = Rd\theta = rd\phi \ ,$$

34

CENTER OF CURVATURE
OF DISHED ELECTRODE

R

R

R

R

R

r

r

r

r

END PIVOTED
ELECTRODE
SUPPORTS
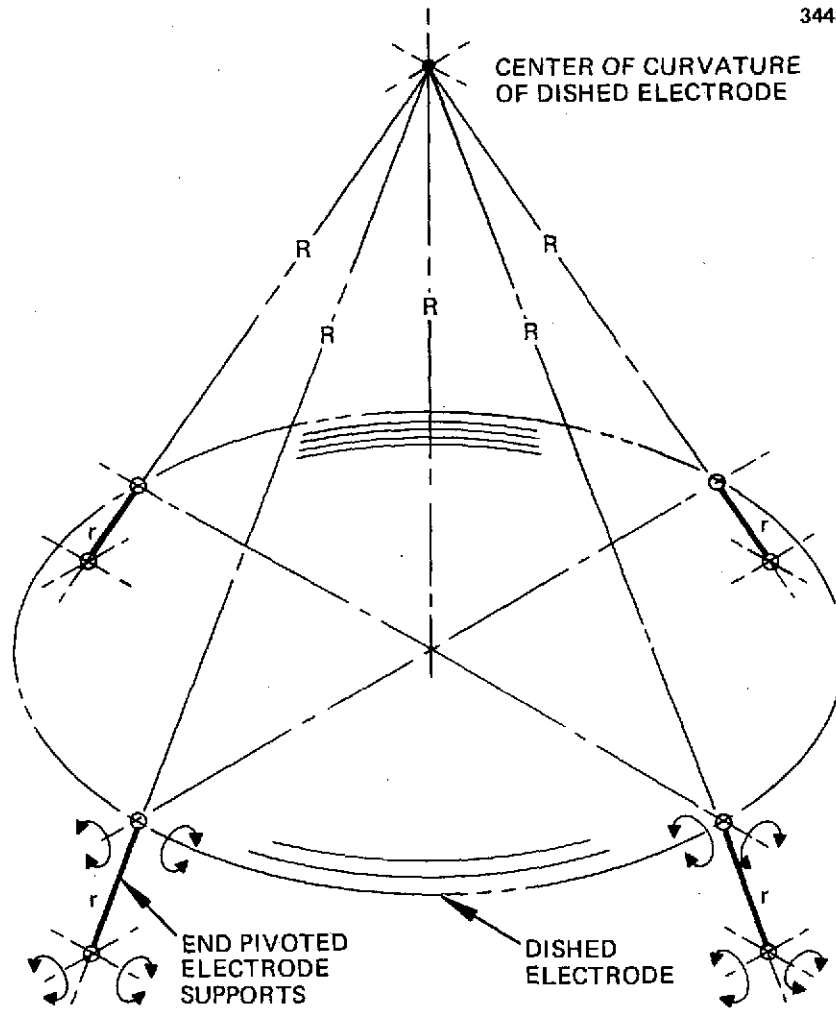
DISHED
ELECTRODE

Fig. 10. Electrode support system for dished
electrode.

CENTER OF
CURVATURE

θ

$\Delta\theta$

R

S

ϵ

ϕ

$\Delta\phi$

r

THRUSTER
AXIS
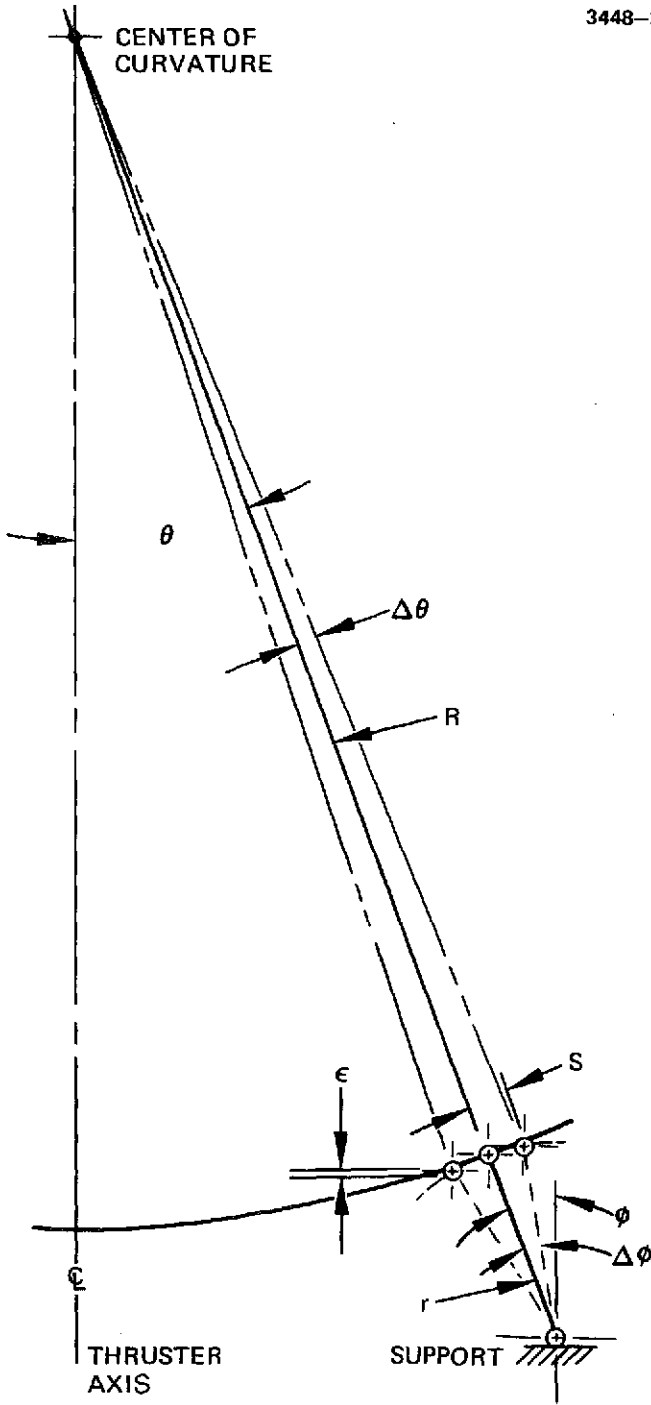
SUPPORT

Fig. 11. Support geometry.

where R is the radius of curvature and r is the length of the link. The angles θ and ϕ are defined by Fig. 11. The deviation, ϵ, of the electrode at the pivot from the desired path is $\epsilon = \Delta R + \Delta r$, where

$$\Delta R = (1 - \cos d\theta) R$$

$$\Delta r = (1 - \cos d\phi) r .$$

A typical value of the deviation, ϵ, is $\epsilon = \Delta R + \Delta r = 0.00066$. This value is based on the following typical values of geometric variables

$$S = 0.051 \text{ cm}$$

$$R = 15.2 \text{ cm}$$

$$r = 2.54 \text{ cm}$$

which result in

$$d\theta = 0.0033 \text{ rad} = 0^{\circ} \, 11' \, 26''$$

$$d\phi = 0.02 \text{ rad} = 1^{\circ} \, 8' \, 43'' .$$

For the four-support system of Fig. 10, when the electrode is moved toward a support, the edge nearest to that support will roll upward while the edge diametrically opposed will roll downward. The deviations, ϵ, of these two supports will always be directed downward. The deviations of the two supports on the other orthogonal axes must also be considered. A two-dimensional view is shown in Fig. 12 where R' and r' are shorter than the unprimed quantities by a factor of $\cos \theta$. If C in Fig. 12 is 10 cm, then $\theta \cong 20^{\circ}$. Deviation at the center supports will be $\epsilon' = 0.00053$ cm, again downwards, in either direction. The difference in deviations of $\epsilon - \epsilon' = 0.00013$ cm, a
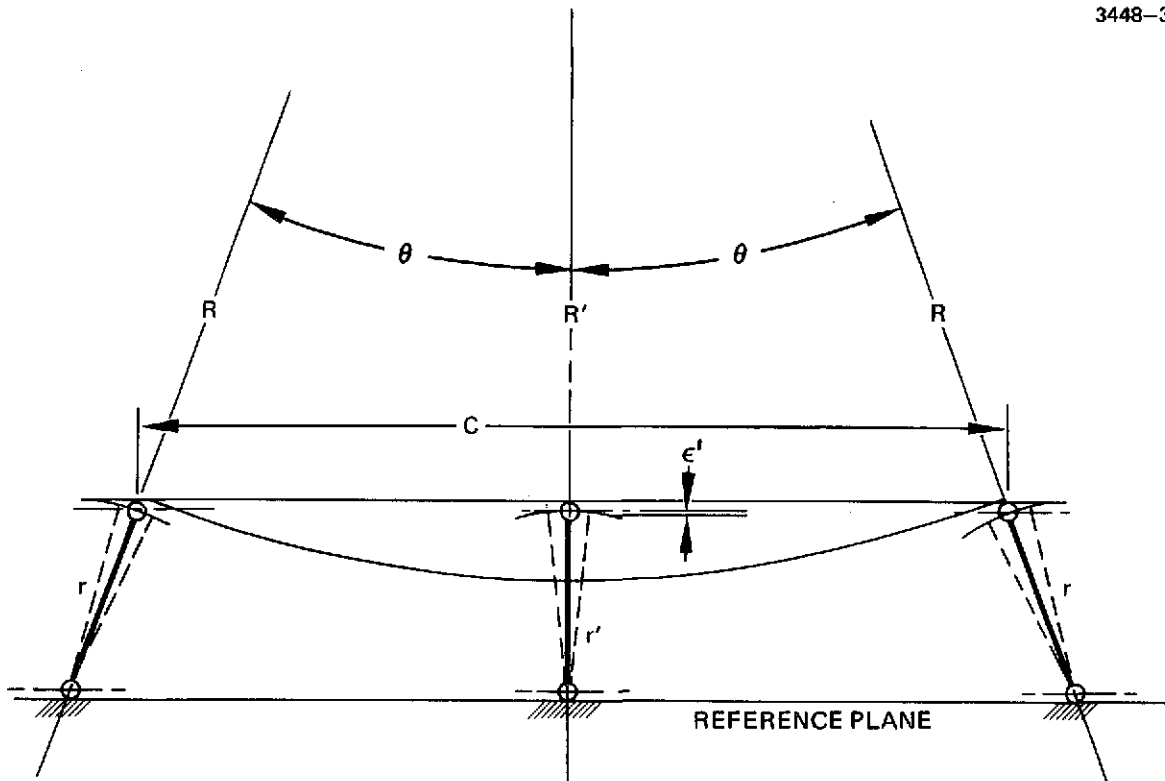
Fig. 12.   Two-dimensional sketch support system.

dimensional mismatch which is so small that it will be absorbed by flexure of the electrode flanges; this will not affect the dished portion of the electrode which is much stiffer.

(2)   Electrode Supports — The moving electrode can be supported by a set of rigid links which have pivots at each end. In such a system, the effects of elevated temperature and of the space environment must be considered. Two design solutions are presented in this section which utilize the elastic properties of materials to provide pivots which avoid these problems, because they do not depend on rotating or sliding parts.

(a)   Rigid Links — Flexural pivots consisting of two flat leaf springs (positioned at 90° to each other) provide zero friction and zero error movement over small angular deflections. The pivot center is located at the intersection of the two leaves. A flex-pivoted, rigid-link, electrode mount is shown in Fig. 13. One flex pivot is used at each end of the rigid link. To furnish freedom for electrode movement along the other orthogonal axis, four more flex pivots are used. Figure 13 shows an actuator using the rigid link as a motion-amplifier transmission. The driver must be mounted to the frame which is itself supported by flex pivots so that it too may rotate to conform to the movement of the electrode. The flex pivots shown in Fig. 13 are commercially available products designed to be installed by clamping in cylindrical holes.

Since the flex pivots act as springs, work is required to rotate them. For the Bendix Model No. 5004-600 and 6004-600 flex pivots examined for this application, a torque of 1.13×10^{-2} Nm/rad is required. For the $\Delta\phi$ of 0.02 rad, a torque of 2.3×10^{-4} Nm is required per flex pivot. Twelve flex pivots are employed per axis, for a total per axis restoring torque of 2.7×10^{-3} Nm. The load bearing capability of a single flex pivot, as stated by the manufacturer,[14] is 56.6 N in tension and 39.1 N in compression.
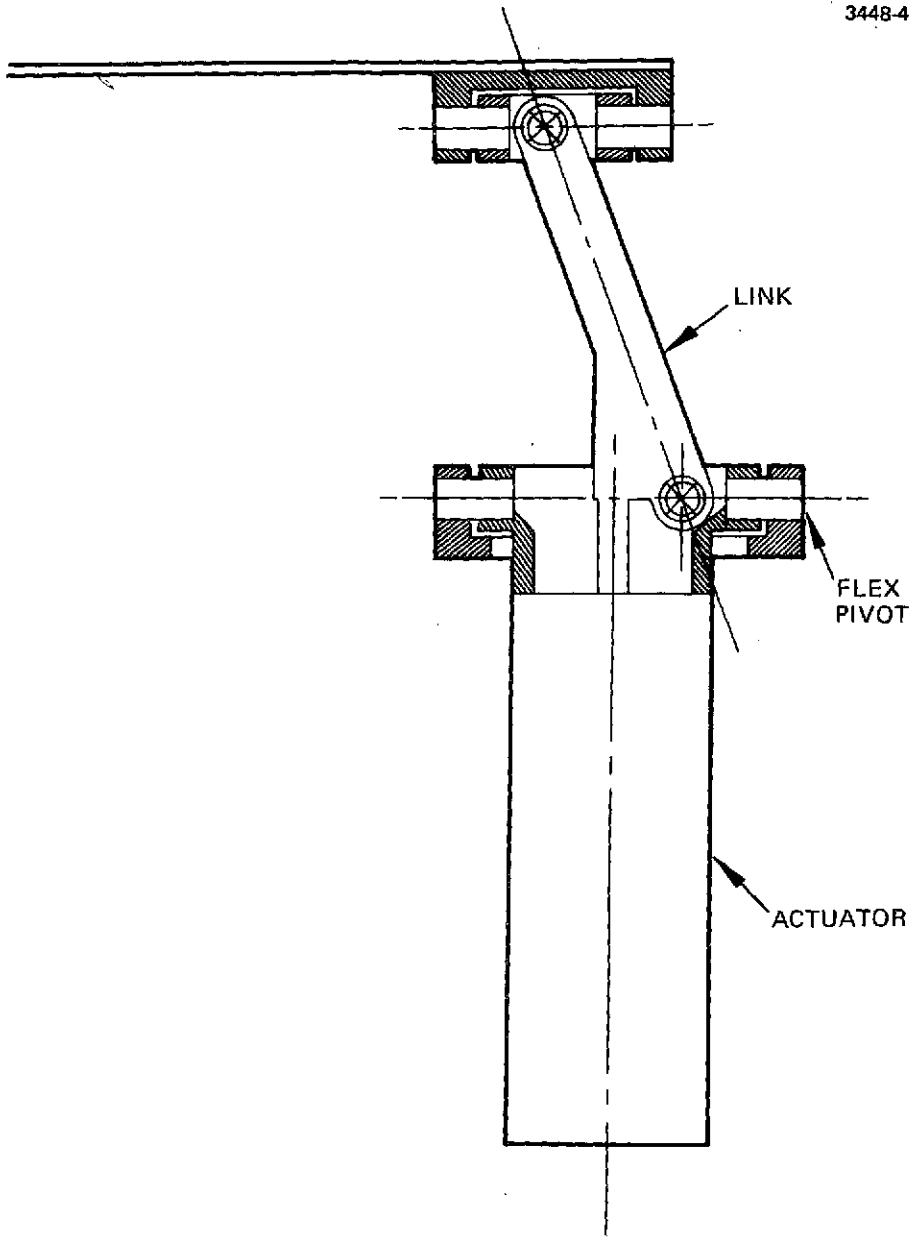
LINK

FLEX
PIVOT

ACTUATOR

Fig. 13.   Flex-pivot rigid-link design.

(b) Column Flexures — An alternative electrode mount is shown in Fig. 14. A round spring-tempered wire is used as a column support. The ends of the column are rigidly fixed. When the electrode is moved, the column bends in a shallow S-shape. The force required to bend the column and the critical load on the column are shown in Table VII for three different wire diameters. For each example, the displacement is 0.051 cm and the length is 2.54 cm.

TABLE VII

Restoring Force and Load Bearing Capacity
for 2.54 cm Wires of Varying Diameters

Wire Diameter, cm	Restoring Force, N	Critical Load, N
0.051	0.236	38.5
0.064	0.573	94.2
0.076	1.187	195.4

T1356

(c) Choice of System — The relative merits of the two electrode-suspension systems can be evaluated by the load bearing capability and the forces required to overcome the resistance of the springs. Assume an electrode of 0.127 cm thickness, 12.7 x 12.7 cm square, with an 8 cm diameter aperture boundary, and with a 50% open beam-extraction region. The weight of this electrode will be 1.73 N. Assume that support attachments will increase the supported weight of the electrodes to 2.2 N. Since four supports are used, each support bears 0.556 N, in a 1 G environment. During a 100 G launch environment, the load for each support increases to 55.6 N. This load can be accommodated by a single flex pivot which can sustain a 55.6 N load, or by a 0.064 cm diameter column which has a critical load capacity of 94.2 N.
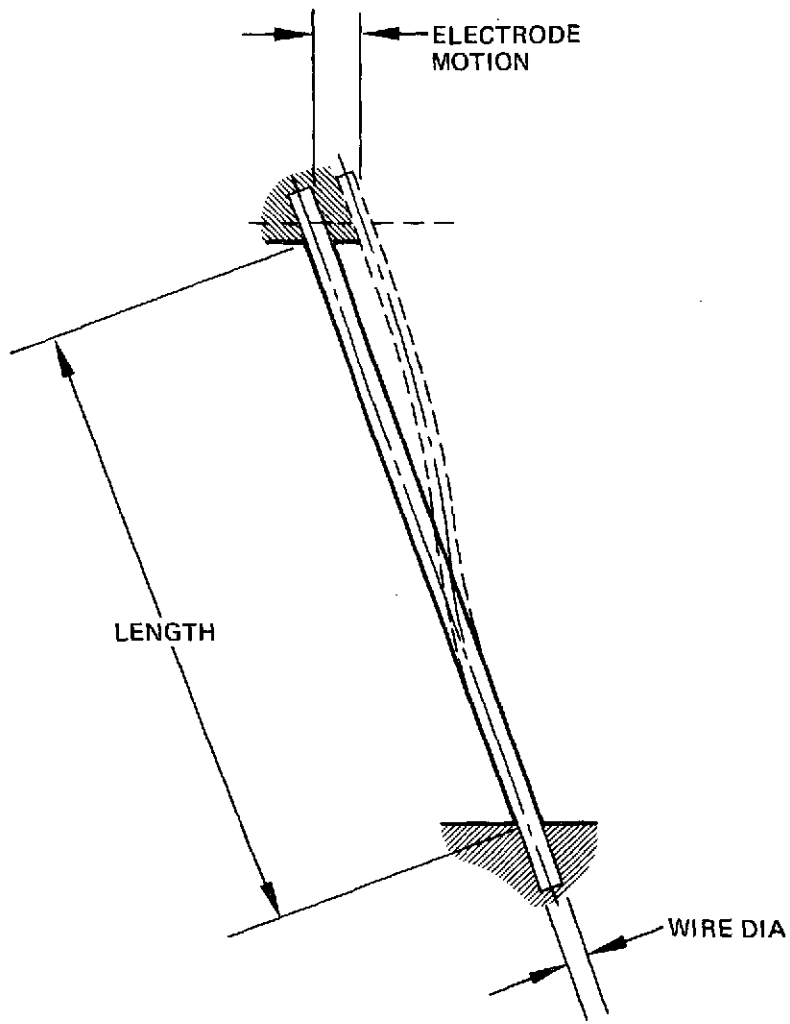
41

ELECTRODE
MOTION

LENGTH

WIRE DIA

Fig. 14. Wire column support.

42

To facilitate laboratory testing, the DGVS should be capable of operating in any orientation in a 1 G environment. Table VIII shows the forces that the driver must overcome in a 1 G environment.

TABLE VIII

Forces Required to Displace Electrode
Operating in a 1 G Environment

Load Description	Suspension System Type	
	Flex-Pivot Link	Column
Weight of electrode, N	1.733	1.733
Weight of support attachment, N	0.489	0.489
Restoring force of suspension system, N	0.106	2.294
Force of additional flex-pivots for transmission, N	0.0 (Included in suspension)	0.018
Total force required at electrode	2.328 N	4.534 N

T1357

b.   Actuator Devices

Various devices have been analyzed which have the capability of producing the required force and displacement. These devices are classified as electromechanical, thermal, and piezoelectric actuators. Where possible, response time, size-weight, and power required have been calculated. Table IX summarizes the performance of these actuator systems.

No particular actuator type listed in Table IX stands out uniquely as offering superior characteristics to alternative selections; some alternatives require high power, some offer limited displacement, some are unduly temperature sensitive, etc. On the basis of

43

TABLE IX

Actuator System Performance (Typical Design Configurations)

Actuator Type	Force, N	Displacement, cm	Power, W	Response		Transmission Ratio Required	Comments
				Actuate	Deactuate		
Stepper-motor driven cam	13.3	0.018	30 Pulsed	10 ms per pulse	10 ms per pulse	3 to 1	Requires bearing development for elevated temperature and vacuum.
Parallel ribbon electromagnet driver	13.3	0.018	-30	50 ms	50 ms	3 to 1	Requires solenoid or electromagnet development.
Piezoelectric stack	311.1	0.0018	<2	10 ms	10 ms	3 to 1	Displacement limited — capable of large force — temperature limited to 265°C.
Rod and tube thermal	22.2	0.010	3	1/2 min	9 min	5 to 1	Simplest fabrication, design.
Volumetric expansion thermal	13.3	0.018	0.5	1/2 min	4 min	3 to 1	Smallest size. Probably best thermal device. Fabrication critical. Maximum teperature, 320°C.
Vapor pressure	22.2	0.010	18	1/2 min	13 min	5 to 1	Susceptibility to leakage.
Bimetallic cantilever		0.051	4.5	1/2 min	11.5 min		Limited force.
Bimetallic Belleville washer stack	13.3	0.018	4.2	1/2 min	18 min	3 to 1	Thermal resistance between disks must be minimized.
Piezoelectric bimorphs	4.45	0.051	<2	20 ms	20 ms	1 to 1	Force and displacement limited temperature, limited 265°C maximum. Large package size.

T1358

44

this analysis and subsequent meetings with the NASA Project
Manager, a stepping-motor-cam-drive system was chosen for design
under the subject contract. The screen accel grid was to be supported
by flexure-column supports. Column flexures were to be predeflected
to keep the grid in contact with the cam actuator. It was hoped that no
power would be required to hold the grid in any vectored position. A
discharge-chamber gimbaling system using screw jacks or a rotational
geared down system was also designed under the subject contract.

2.   TGS Design

A plan view of the TGS was shown in Fig. 4 of this report. In
the TGS layout, the thruster support plate is bolted to central circular
ring at eight locations. The ring in turn is supported from shafts
projecting from the center races of two sets of ball bearings. The
other races are connected to a full-circular yoke which is itself sup-
ported at the two orthogonal locations by a similar pair of bearings
supported by the mounting flanges of the gimbal system.
A linear actuator is also supported from one of the two
mounting flanges which is used to tilt the thruster flange about the two
outermost bearing sets. A second linear actuator is mounted directly
from the full-circular outer yoke which is used to tilt the thruster
flange about the axis of the two innermost bearing sets. The linear
actuators are adapted from an existing flight qualified device which
was developed by the Hughes Space and Communications Group for use
as an Intelsat IV antenna positioner. Success of the positioner has
been demonstrated on the first Intelsat IV which was placed in orbit in
January 1971. The actuator has a mass of 0.255 kg in the configura-
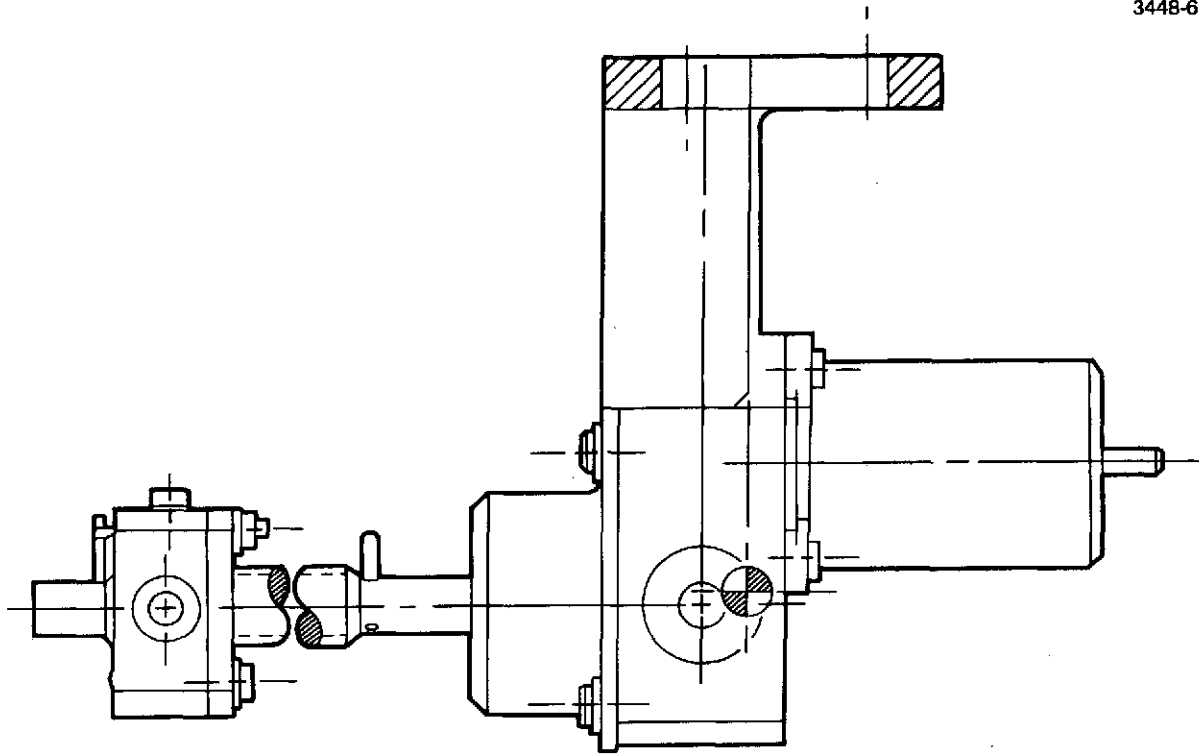tion shown in Fig. 15.

Fig. 15. Flight qualified linear actuator.

a.   Linear Actuator Description

Actuators are installed on the gimbal assembly, such that linear motion of the actuator, acting at a radius arm, produces the antenna angular orientation. Each motor is mounted to an aluminum gear box which houses the bearings, shaft gear and jackscrew shaft. Sequentially ordered pulses cause the selected motor to advance one 15 degree step for each pulse. The motor pinion, a 64 pitch, 18 tooth anodized aluminum gear, meshes with the 72 tooth aluminum gear pinned to the jackscrew shaft.

The jackscrew shaft, of 7075 T6 aluminum, rides in two "Bartemp" bearings contained in the gear box case. The aluminum gear teeth and the threads of the jackscrew are treated with an inorganic bonded solid lubricant ("LUBECO 905"), and burnished. The bearings contain a reinforced teflon ball retainer impregnated with MoS_2. The races and balls are burnished with MoS_2.

Each 15 degree step of the motor results in a 3.75 degree rotation of the jackscrew. The 0.953 cm diameter jackscrew is threaded with a 16 pitch UNC Class II thread. This threaded end of the jackscrew is engaged in a spherical nut mounted in an aluminum holder, which in turn is held in a "yoke" of the respective structure driven arm, azimuth or elevation. The 3.75^O rotation of the jackscrew results in 0.00165 cm translation of the nut and arm along the axis of the jackscrew. Since the structure arm and "yoke" locate the nut center at 11.905 cm and 14.059 cm from the X and Y gimbal pivot axes, the resultant structure motion is 0.00789 and 0.00688^O respectively per motor step, an overall reduction from motor to gimbal of approximately 2000:1.

The stepper motor utilized is a phase-switched, 3-phase variable reluctance rotor type. Ratings and characteristics of the motor are listed in Table X.

TABLE X

Motor Ratings and Characteristics

Operating voltage	28 ± 7 V dc
Power	30 W maximum at 25°C and 28 V dc
Angular rotation	Bidirectional in increments of $15 \pm 0.75^{\circ}$
Running torque at stepping rate of five steps per second (sps) and nominal excitation (28 V dc)	0.01 Nm minimum at 125°C; 0.017 Nm minimum at 25°C
Operating temperature range	-65 to $+125^{\circ}$C
Storage temperature range	-160 to $+125^{\circ}$C
Motor size	No. 11
Motor mass	0.144 kg maximum

T1359

b.   Bearing Lubrication

The two gimbal rings attached by their associated pivots are shown in Fig. 16. Both rings are fabricated of Type 6061 aluminum. The inner ring weighs 0.070 kg and the outer ring weighs 0.170 kg. Ball bearing pivots have been lubricated for high-temperature space applications by sputter deposition of a MoS_2 film using a process described by Talivaldis Spalvins of LeRC.[15]

High-strength-steel ball bearings were coated with the dry-film lubricant while mounted in the rotating fixture shown in Fig. 17 for sputter-deposition of MoS_2. (The same technique was used successfully for lubrication of bearings employed in the DGVS.) The assemblies were precleaned by hot degreasing and rinsing in alcohol, then blown dry in hot nitrogen. They were inserted into the system on a copper pallet which had previously been sputter-coated with MoS_2. With the first side of each bearing facing up, they were sputter etched for 15 min. at 200 W of RF power (300 V in an argon plasma). The
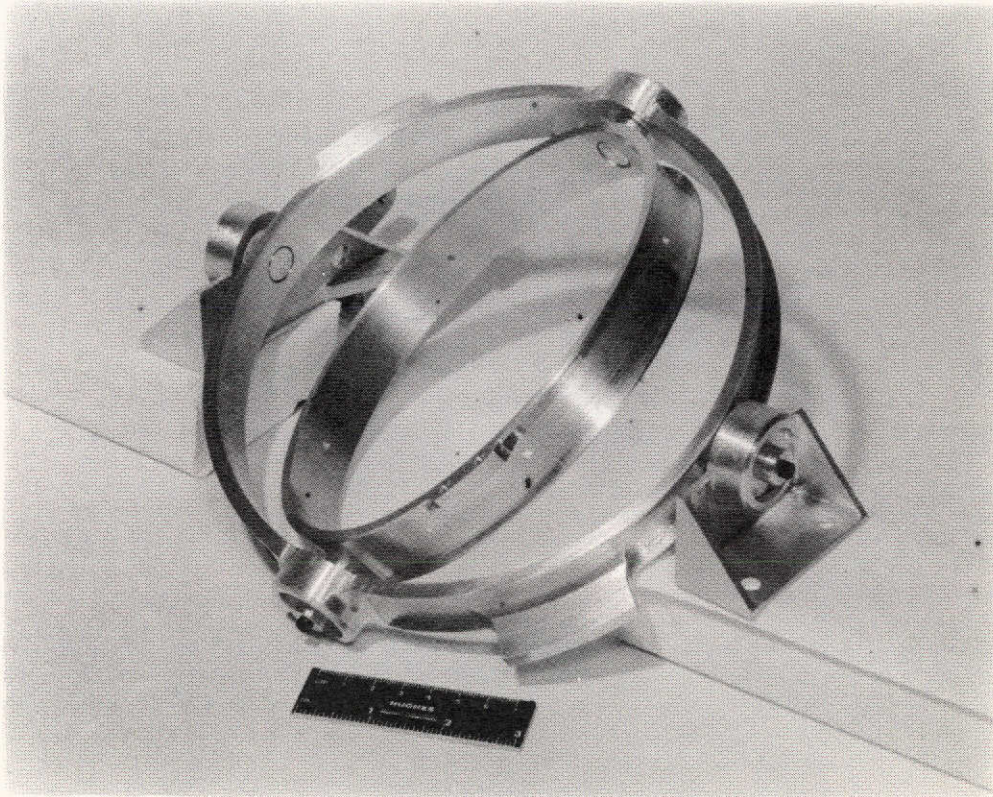
48

M10284

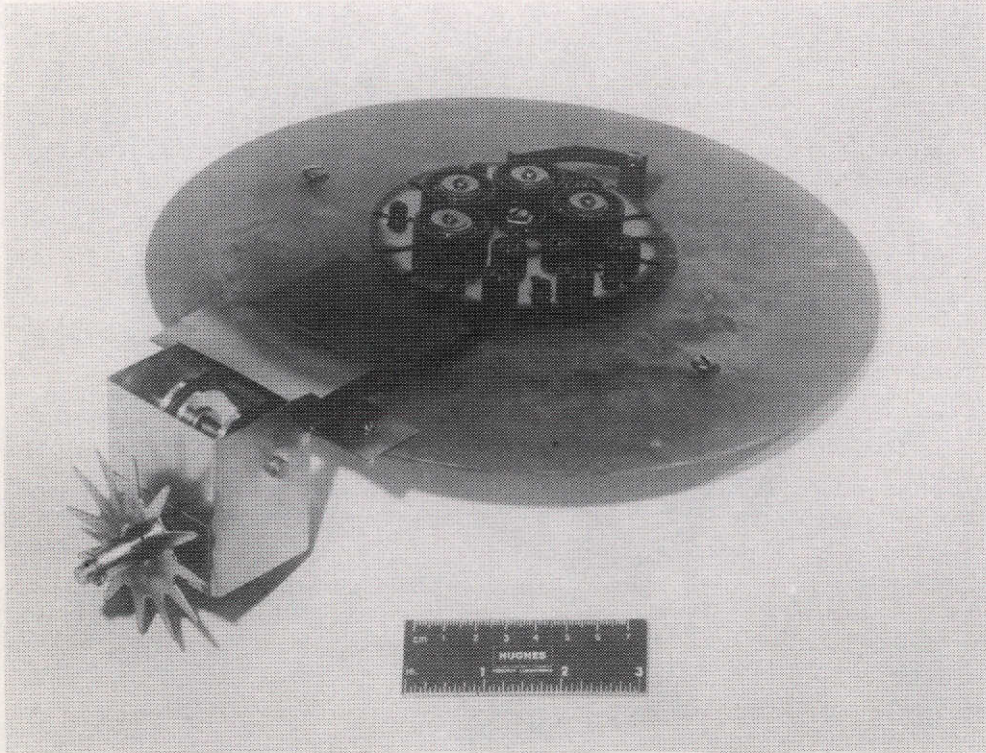Fig. 16. Gimbaling rings fabricated under NASA
Contract NAS3-17791.

Fig. 17. Rotating fixture for sputter deposition of
MoS$_2$ on ball bearing assemblies.

MoS_2 target was then moved into position over the bearings and the material was sputter-deposited for 15 min (500 W of power in argon pressure of 4 μm to give a deposition rate of about 130 Å/min). The deposit was seen to be fairly well distributed on all sides of the bearing assembly but it could not deposit on the part of the balls covered by the retainer ring. Therefore, the inner sleeve was rotated 90° for an additional 15 min deposit and the procedure was repeated 4 times. The bearings were turned over and the etching and the 4 deposition steps were repeated.

Following these deposits the bearings were examined under a microscope and a few small areas of the balls were seen to be uncoated. Hence, they were each spun to give a new random orientation and two 15 min deposits were made with each side up. After this, no open areas were observed. On glass slides which were coated simultaneously with the bearings, the film was very durable and adherent, requiring an X-acto knife to scratch away a portion for measuring the film thickness.

3.   DGVS Design

A layout drawing of the DGVS was shown in Fig. 3 of this report. Figure 18 shows the electrode driving mechanism. The axial location of the moving electrode is maintained by column springs canted inwards toward the spherical center of the electrode dish to approximate a rolling motion about the center of curvature of the dished electrode. Lateral misalignment of the moving electrode is accomplished by the rotation of an eccentrically mounted ball-bearing system working in a close fitting slot. The slot serves two functions. One, it converts the rotating motion into a linear motion and two, it provides freedom for motion along the orthogonal axis.

The eccentric shaft is located on the end of a driveshaft which is supported by two widely spaced ball bearings. The three bearings

51

ECCENTRICALLY
MOUNTED
BALL-BEARING
SYSTEM

COUPLING TO ACCEL ELECTRODE

ELECTRICAL
ISOLATOR

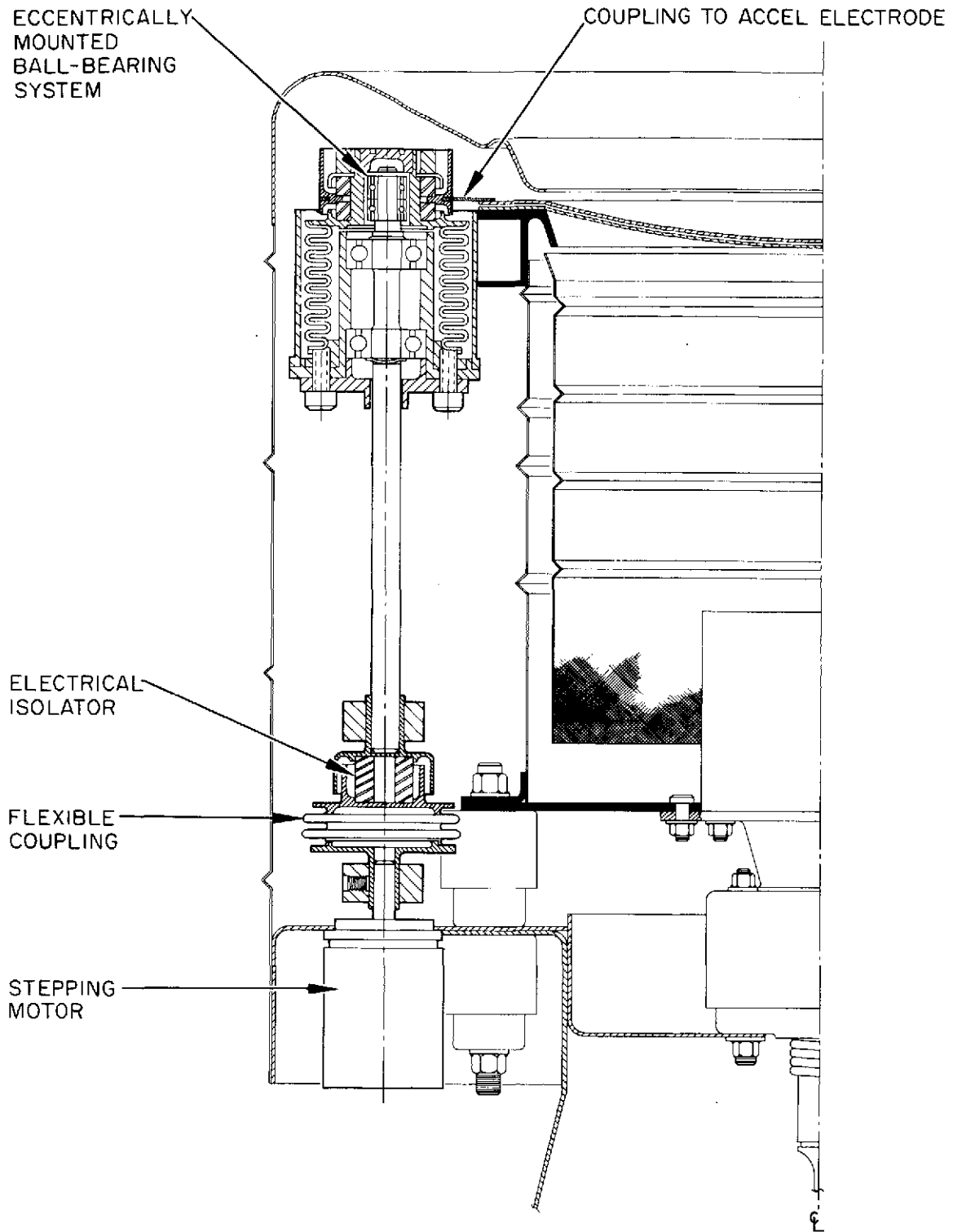FLEXIBLE
COUPLING

STEPPING
MOTOR

Fig. 18.   DGVS drive mechanism (shown attached to 8 cm
thruster).

are protected from sputtered material by a bellows enclosure.* A double shielded electrical isolator is located on the driveshaft. This allows the stepper motor to be mounted on the thruster supporting structure which is at spacecraft potential and operates at reduced temperature. This is essential for the stepper motor, since no stepper motor has been identified that can operate in the temperature environment that exists at the thruster location. The electrical isolator is a ceramic column with brazed, fitted end caps. A switch is actuated by a lobe on the side of the drive shaft which provides a reference position of the electrode. Other positions are determined by counting the number of steps that the stepper motor has been pulsed from that reference position.

Electrode position is not linear with angular displacement of the eccentric, but follows the displacement of simple harmonic motion. Starting from the null position at 0° and 180° of the eccentric the electrode displacement will move $d = \epsilon \sin \Delta\theta$ where ϵ is the eccentricity of the bearing, and $\Delta\theta$ is the angular rotation of the shaft.

Several design innovations are incorporated to achieve high thermal and mechanical stability. The screen and collar polepieces are fabricated as one structure from KOVAR alloy consisting of 29% nickel, 17% cobalt, with the remainder consisting mainly of iron. In the fully annealed condition, this alloy has good magnetic properties achieving a maximum permeability of $B/H_{max} = 3700$ at a flux density $B = 7000$ G (Ref. 16). As annealed, the alloy has a coefficient of thermal expansion of 5.1 to 5.5×10^{-6} cm/cm^{O}C over the temperature range 30 to 450^OC; this compares closely with the coefficient for molybdenum which is 5.1×10^{-6} cm/cm^{O}C over the same temperature range.[16] The Curie point for the alloy is 435^OC (Ref. 16). The

---

*Under the subject contract, sufficiently compliant bellows could not be purchased in time to meet the fabrication schedule. Accordingly, shadow shields were used in place of the bellows enclosures in actuators fabricated under this contract.

DGVS configuration is capable of maintaining very precise tolerances in the position of the screen electrode relative to the accel electrode. This is accomplished by the use of indexing features which fix the position of the two extraction electrodes with respect to the stable toroidal structure formed by the screen-collar polepiece.

In the original DGVS design, a gear box was to be used to reduce the 90° step of the stepper motor to 1.8^O rotation of the shaft. This required a 50:1 reduction. This reduction could have been accomplished in a single stage by using worm gears, while two stages would have been required using spur gears. The inherent wiping action between the worm and the worm gear, however, would have required a reduced temperature environment where a sealed gear box for oil or grease lubrication would be appropriate. Spur gears with an involute tooth form, on the other hand, do not require the critical lubrication of worm gears, since they operate on a rolling action between the teeth. This provides a greater assurance of meeting the life requirements using dry lubricants, and thus dry lubricated spur gears were chosen. After review by the NASA Project Manager, however, the DGVS system was modified to eliminate the spur-gear transmission system in order to reduce system mass. This modified system performance from its earlier design capability for deflection from -10° to $+10^O$ in 200 increments of 0.10^O beam-deflection each to a diminished design capability of -10° to zero to $+10^O$ in 10 increments of 2^O each.

4.   TGS Performance

The thruster gimbaling system was evaluated by investigating the directional change of the thrust vector as a function of motor-step number. Directional change is accomplished by gimbaling the entire thruster (not including propellant tankage) about either of two orthogonal axes. The thruster and gimbal system are shown in Fig. 19. Two linear actuators were used to tilt the thruster about the two orthogonal
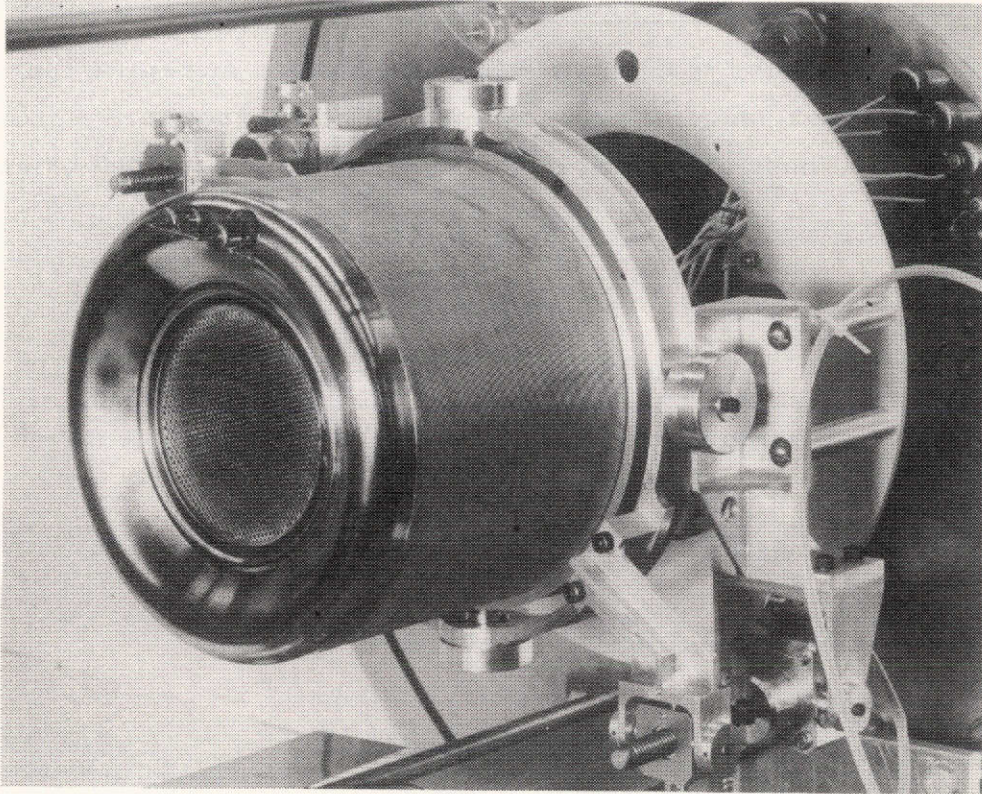
M10329

Fig. 19.   8-cm thruster mounted on gimbal system.

axes of the gimbaling system. A control circuit permits the motor to step the thruster along either axis automatically by a predetermined number of counts or by single counts in a manual mode.

a.   Pretest Measurements

Prior to evaluation of the vectoring system in the vacuum chamber, several pretest performance parameters were determined. These are listed in Table XI and are described briefly below.

TABLE XI

Pretest Performance Parameters

Vectoring power requirements (each axis)	2.4 W (12 V dc, 0.2 A for each motor)
Time response of vector drive system ($-10°$ to $+10°$)	1 min
Vector system mass	1.23 kg
Vector system driving force — Y-axis, X-axis (on motor in line with worm gear)	24.5 N, 16.7 N
Distance between the gimbaled center-of-mass and center-of-rotation	6.7 cm

1360

Each motor was designed to operate at 28 V dc, but only for short term operation. Since power is continually applied to the units in the gimbal application, the operating voltage was decreased to 12 V. to minimize the heat load. This voltage is adequate for the motor operation and causes the operating temperature to be lower. Each motor draws 0.2 A at all times to provide positive locking action.[*]

*Where zero-power locking is required, the motors can be obtained with electromagnet-actuated brake disks.

56

Tests in air showed that the motor temperatures rose to 40°C, while they rose to 90°C while testing in the vacuum chamber. The time response to gimbal from -10° to +10° was determined for each axis; this was 60 s for the Y-axis and 65 s for the X-axis. The vector system driving force was determined by the force required to stall the driving motors. The measurement was made by measuring the opposing force at the motors in line with the worm gears that drive the gimbals.

b. Gimbal Vector Measurements

The thrust vector measurements were made with the thruster set at the values shown in Table XII. All beam-deflection measurements were performed in a 1.2 m-diameter vacuum chamber at a pressure of less than 4×10^{-6} Torr. The motors responded as expected and reached an operating temperature of 90°C. The temperature of the gimbal system mount nearest to the thruster reached 60°C. Two probes were used to measure the current-density contours required to establish the centroid of the thrust vector. The probes consist of 36 cm long, 0.64 cm diameter stainless steel tubes which are swept about orthogonal axes across the ion beam. Figure 20 shows how these probes are oriented with respect to the beam. The probes were located about 46.7 cm from the face of the thruster. At this distance, a beam vector angle of 1° results in a linear displacement of 0.76 cm. The centroid location was determined by the intersection of the angular measurements for maximum intensity of each probe. The intensities for each probe were recorded as a function of angle on an X-Y recorder, and a typical plot of zero deflection is shown in Fig. 21. A plot for a west deflection of 5° is shown in Fig. 22. Data were obtained for north, south, east, and west deflections. The significance of these directions are shown in Fig. 23 as one faces the thruster. The accuracy of the data appears to be within 1° and showed less than 1° drift for the zero (undeflected) position. Several zeros were recorded during the thrust vector gimbaling test; these are plotted in Fig. 24. All points that lie within the circle in Fig. 24 are less than 1° from each other. It can be seen that the thruster vector returned to within 1° of the original zero after being gimbaled.
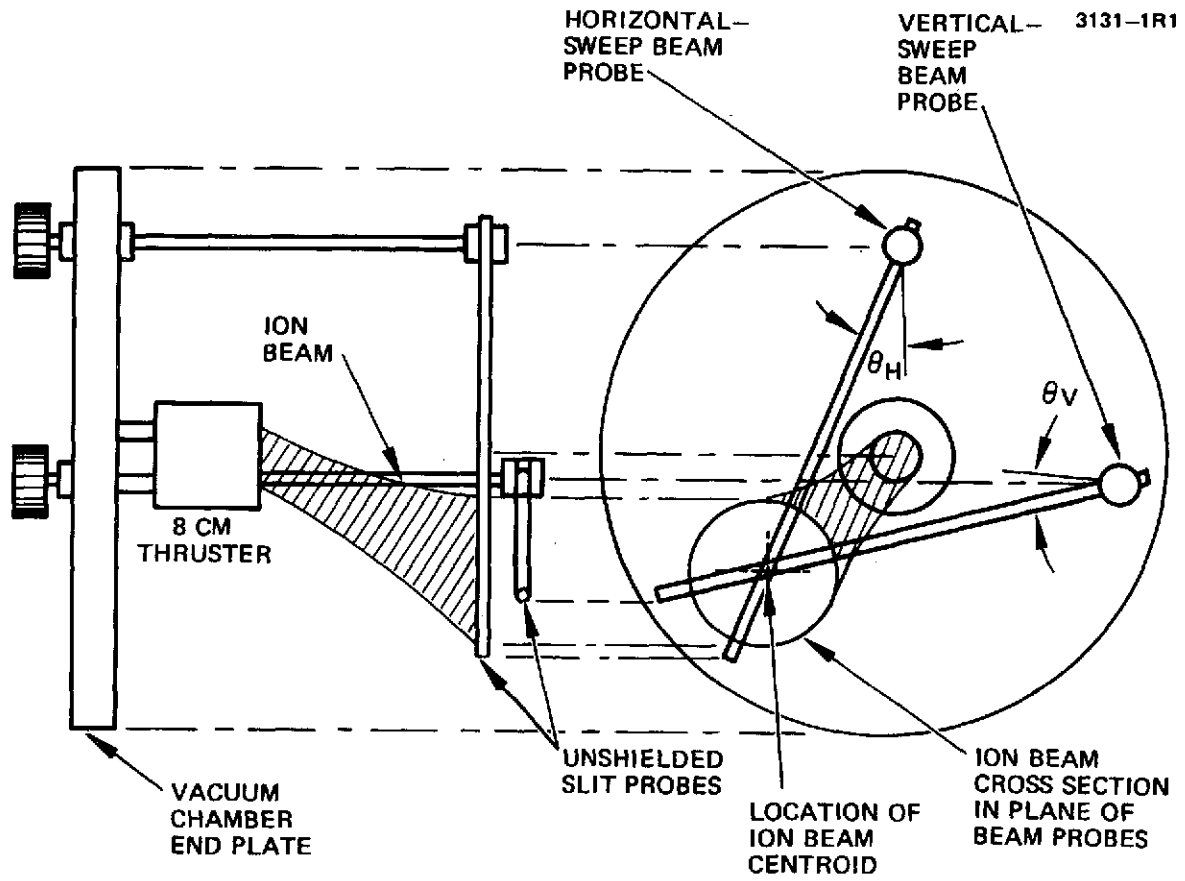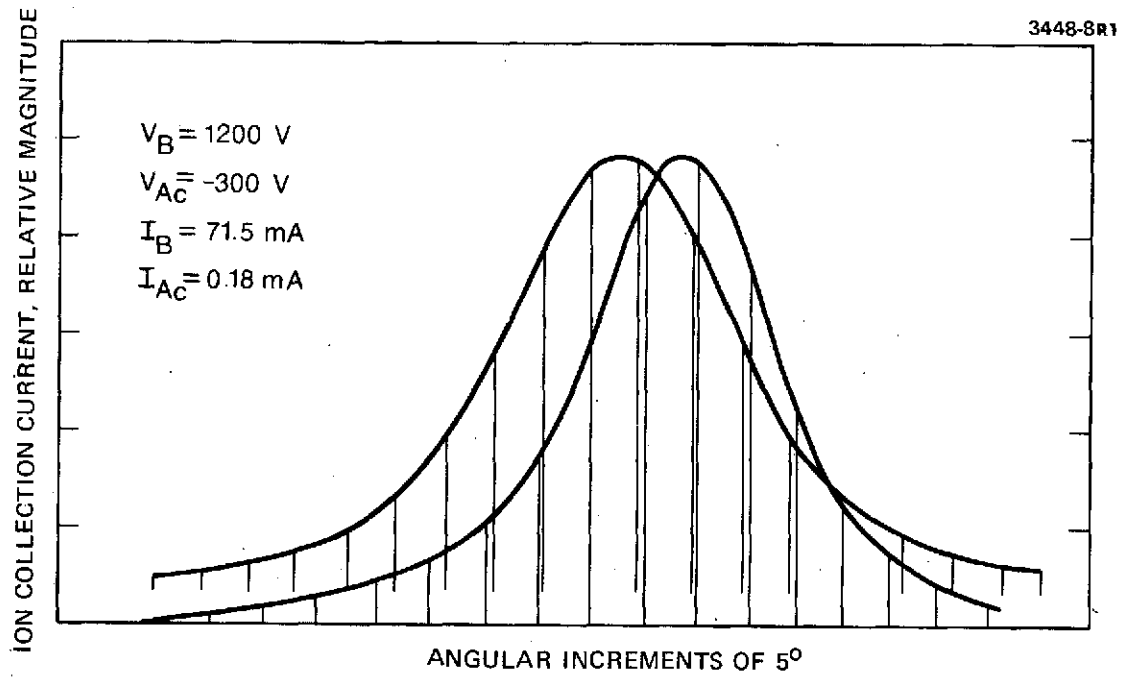
Fig. 20. Probe configuration.

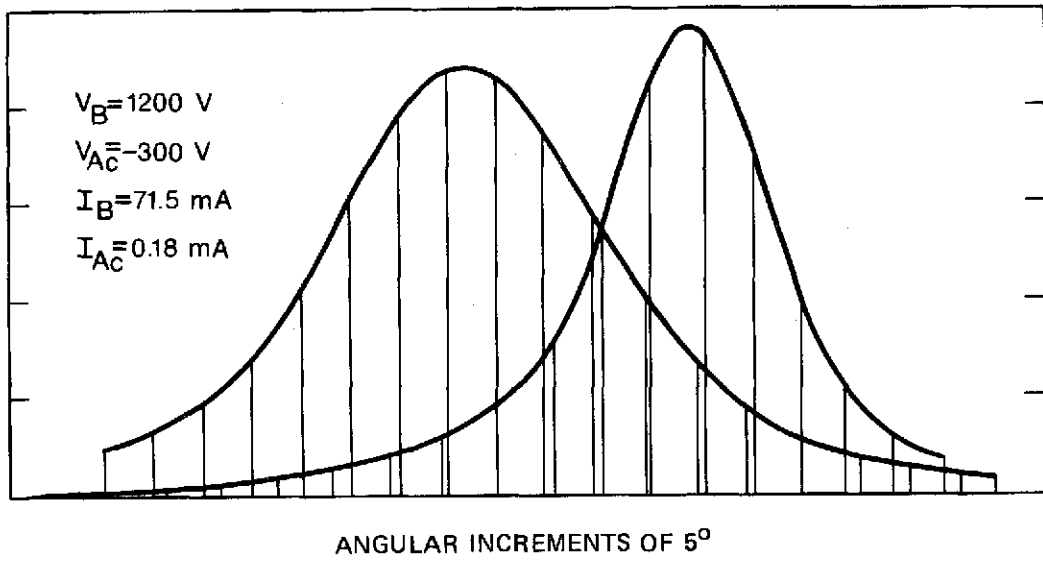Fig. 21. X-Y plots of beam scans for zero deflection.

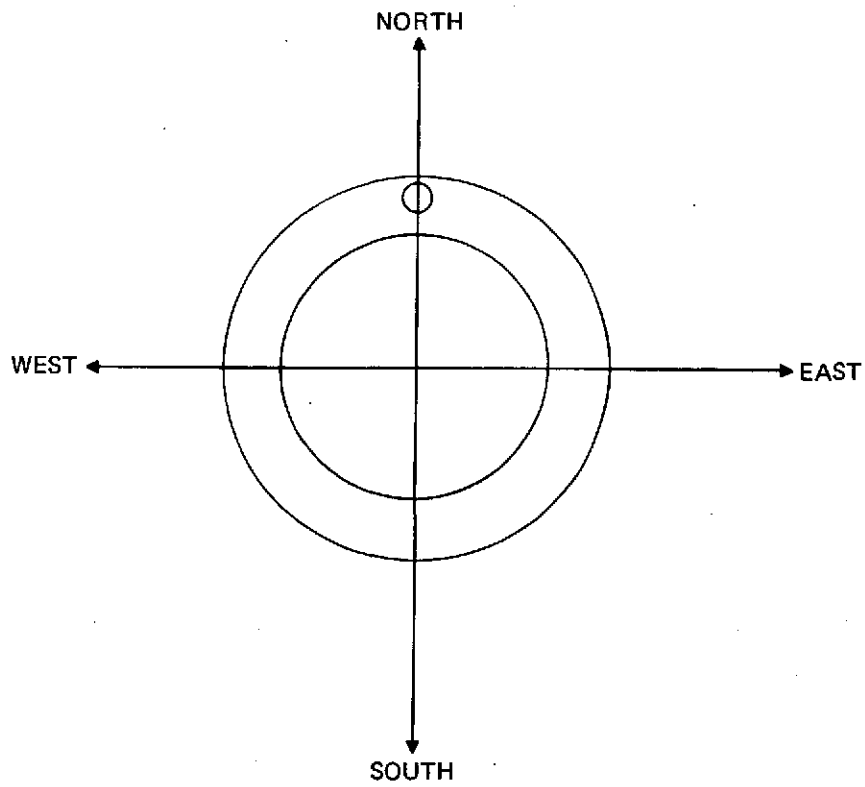Fig. 22.   X-Y plots of beam scans for 5° west deflection.

Fig. 23.   Thruster front view nomenclature used
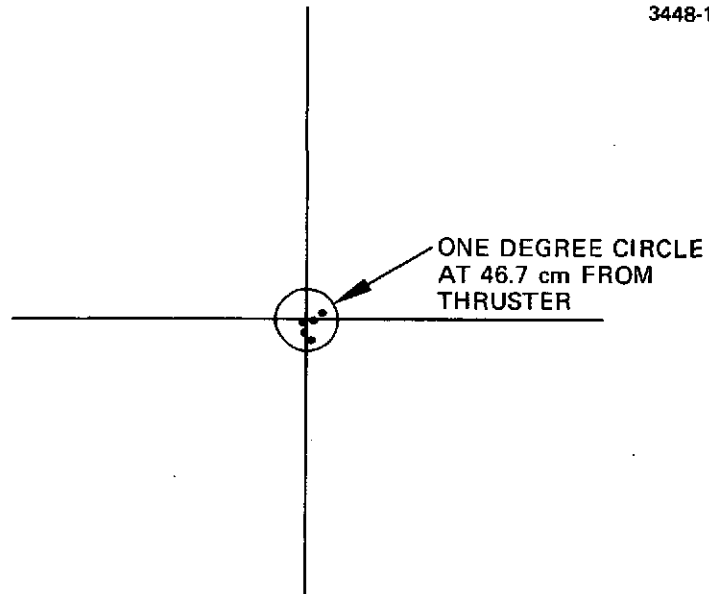   for vectoring measurements.

Fig. 24. Centroid for zero deflection
46.7 cm from thruster. (Scale
= 1x).

TABLE XII

Thruster Operation Setpoint

Beam voltage, V_B = 1200 V

Accel voltage, V_{Ac} = -300 V

Beam current, I_B = 71.5 mA

T1361

Data taken during this period are shown in Fig. 25. The values are read in the following way: The X-axis in the figure indicates the motor counts. These counts could generate either X or Y movement for the thruster depending upon which motor is being used. The Y-axis in Fig. 25 shows the thrust vector deflection obtained from the probe data. Deflections of greater than 10° were obtained in all four directions. The data is reproducible to about 1°. The N-S and E-W deflection data lie along a straight line and are orthogonal to within a few degrees. This slight nonorthogonal behavior is not fully understood at this time; initial investigation indicates a high degree of orthogonality in the behavior of the gimbal system itself.

c.   Vectoring Performance Parameters

Performance parameters of the 8-cm thruster with the gimbal system do not change as the thruster vector is varied. This is true because the entire thruster assembly is moved as the thrust vector is changed. For this reason, performance parameters were recorded at a vector angle of 0° only.

Data were taken for three different ion beam currents. These values were I_B = 72 mA, I_B = 54 mA and I_B = 36 mA. The first set of data to be discussed is an investigation of the accelerator-drain current as a function of total extraction voltage. Total extraction voltage equals the sum of the absolute values of the beam and accel voltages (i.e., $V_{total} = |V_B| + |V_{Ac}|$). These data were taken at a
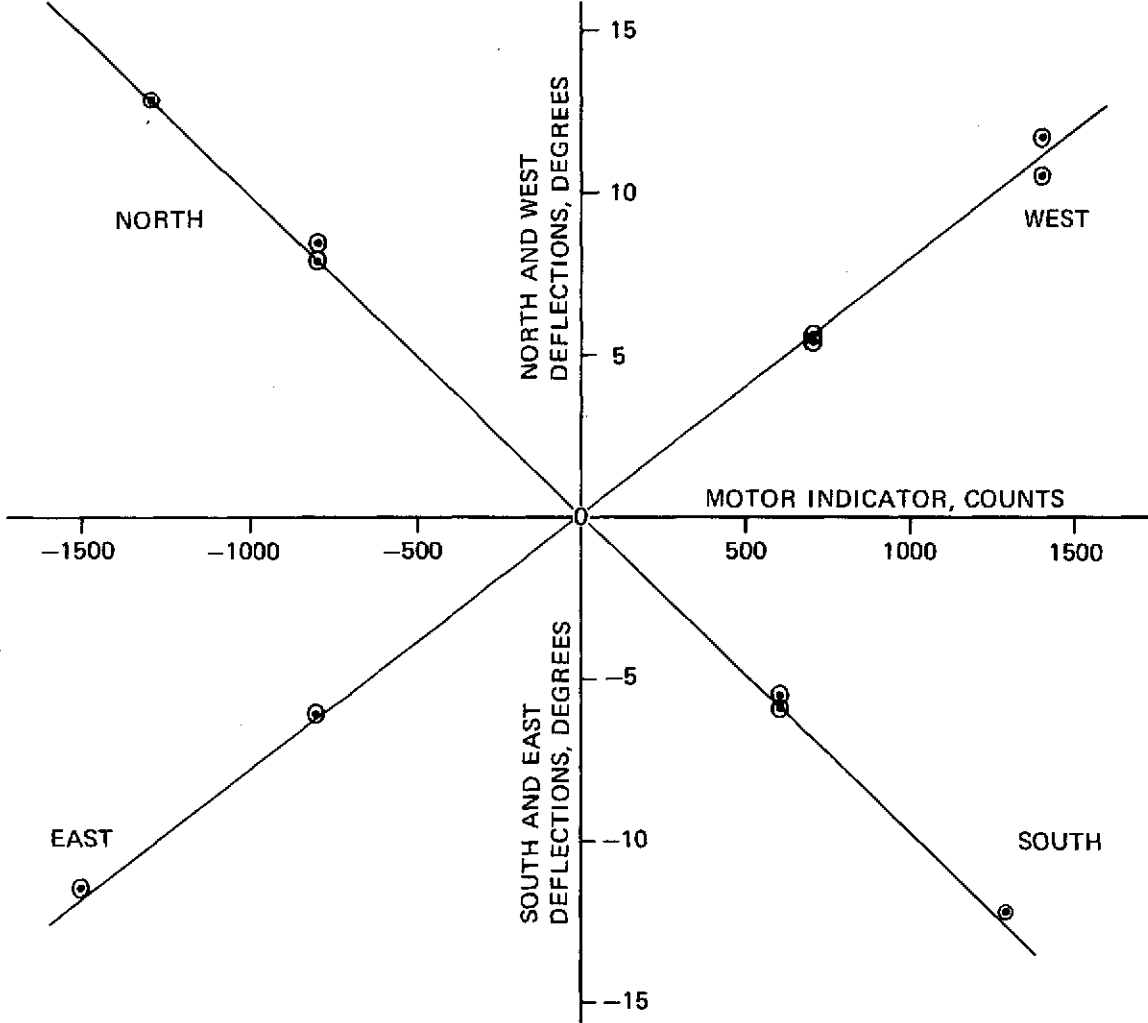
63

Fig. 25. Direction of thrust vector as a function of
motor steps.

constant beam-to-total accelerating potential ratio of 0.8, and are shown in Fig. 26. In all cases, the beam currents and accel currents are relatively constant in the 1000 V to 2000 V region. The nominal operating point for the thruster is V_{BEAM} = 1200 V and V_{Ac} = -300 V; this point is in the middle of the flat sections of the curves. The beam currents start to drop and the accel currents start to increase as the total voltage decreases to 500 V. The onset of electron backstreaming occurs at about 400 V and shows up as a false beam current reading.

The second set of data examines the accelerator drain current as function of the ratio of beam-to-total accelerating potential. These data were taken at a constant total extraction voltage of 1500 V. Fig. 27 shows that the different current levels behaved in a similar manner. The current values were flat from the lowest ratio, 0.5, measured to the ratio of 0.87. The ratio approaching unity means that the Accel voltage was approaching zero; this permits electron streaming and appeared as a false beam current. The nominal operating point for the thruster has a ratio of 0.8 and is below the onset of electron streaming. Based on the data shown in Figs. 26 and 27, the design point V_B = 1200 V and V_{Ac} = -300 V, and V_B/V_{total} = 0.8 is acceptable and falls within the safe operating region.

5.   DGVS Performance

The Dished Grid Vector System (DGVS) was evaluated in the configuration shown in Fig. 28, by investigating the directional change of the ion beam thrust vector. Directional change is achieved in this device by displacing the accel electrode relative to the screen electrode in either of two orthogonal directions; displacements are made with two stepping-motor cam-drive actuators. The accel grid is supported by flexure-column supports which are predeflected to keep the grid in contact with the cam actuators. The East to West (E-W) movement is performed in twelve steps while the North to South (N-S) movement is accomplished in eleven steps.
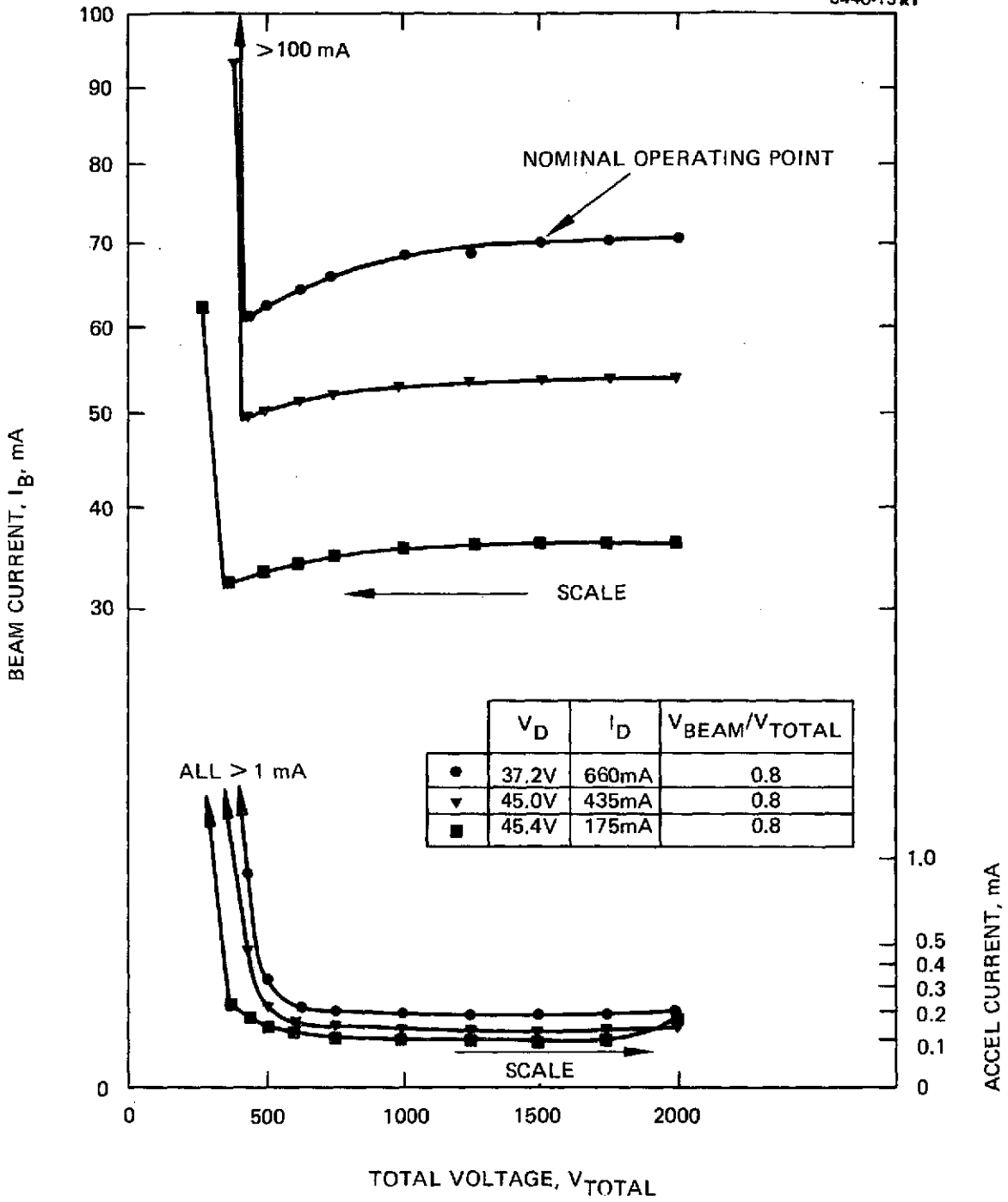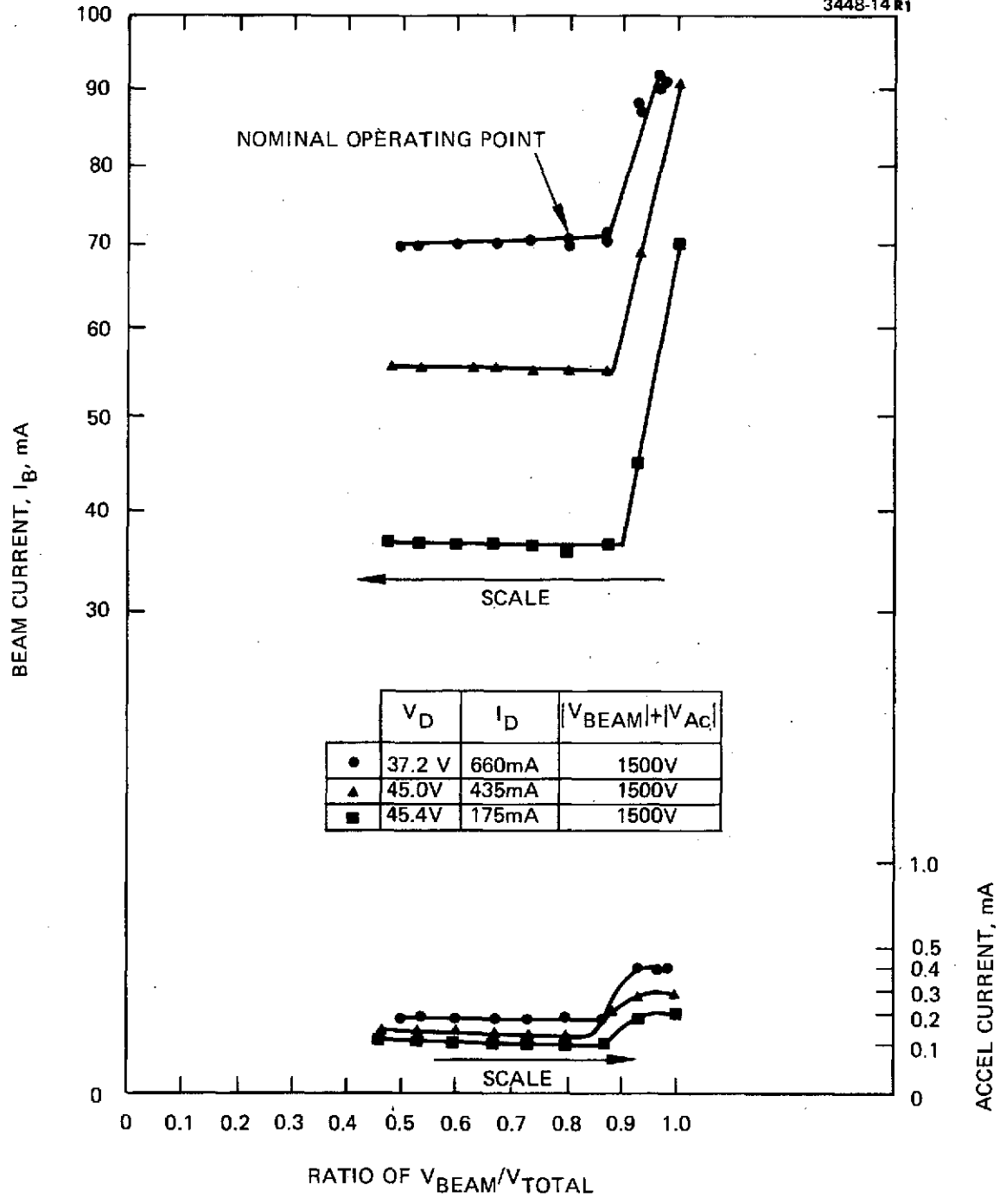
Fig. 26. Beam current versus total voltage.

66

Fig. 27. Beam current versus V_{beam}/V_{total}.
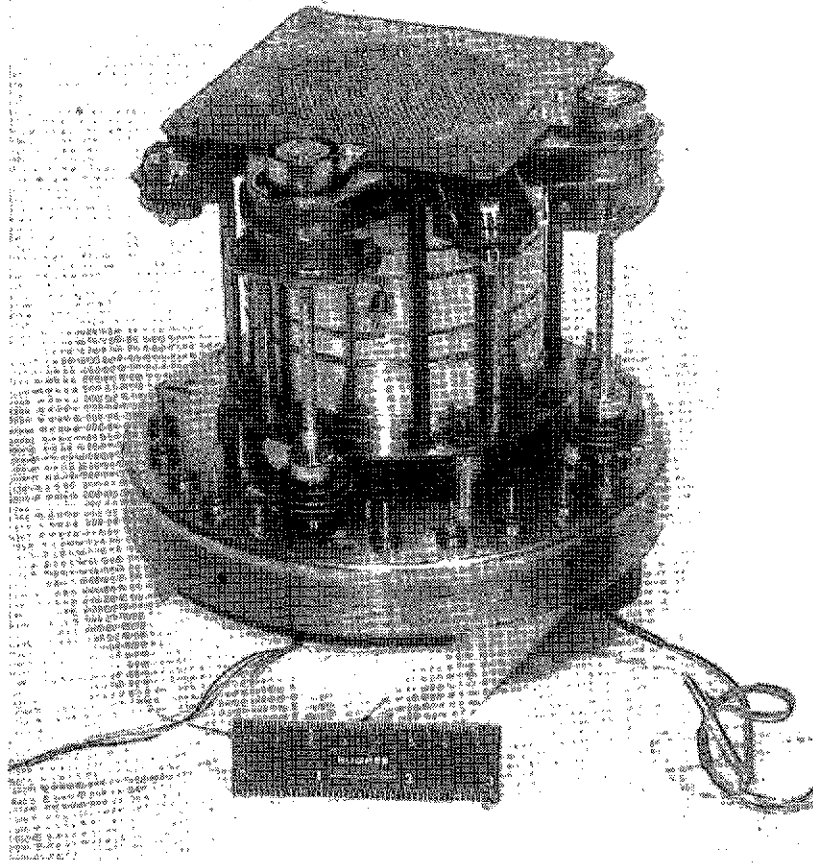
Fig. 28. DGVS attached to 8-cm thruster.

a.   Pretest Measurements

Before the DGVS was tested for vectoring properties, several pretest performance parameters were determined. These are listed in Table XIII and are described in more detail below. Two different sizes of motors were used, in order to evaluate motor-torque requirements. For reasons of economy, low cost motors were selected by the NASA Project Manager for the DGVS application which were of a normal off-the-shelf variety and which were not especially designed to operate in a vacuum environment like those employed in the TGS configuration. Power is applied both for movement and for holding; and during in-vacuum operation, both motors tended to heat up. The operating voltage for each motor was determined by lowering to the lowest values that would assure repeatable operation of the motors. With the power settings in Table XIII and with the thruster at the nominal operating point, the temperature of both motor cases approached $100^{\circ}C$ in about 10 min. Above this temperature, the motors would not function. If the power to the motors was turned off, their temperatures would drop, and they would become operational for a short time. Data were taken only during these short intervals of time. Typically, a 10 min interval of data taking would be followed by a motor power-off period of 1/2 to 1 hour.

TABLE XIII

Pretest Performance Parameters

Vectoring power requirements (12 V, 0.4 A for E-W motor size No. 8, Model 008-080-6, IMC Magnetics Corp., Maywood, Calif.) (20 V, 0.165 A for N-S motor size No. 11, Model 011-082, IMC Magnetics Corp., Maywood, Calif.)	5.1 W
Time response of vector drive system (maximum angle one direction to maximum angle opposite direction)	5 s
System mass (including the thruster shell, beam-extraction system motors and drive system, but not including a CIV or ground screen)	1.1 kg

T1362

b. Vectoring Measurements

Thrust vector measurements were made with the thruster operating at the values shown in Table XIV. The indicated variations in voltages and current settings were considered to be sufficient for investigation of their effect on the deflection angles. The measurement technique used two probes to measure the current-density contours to establish the centroid of the thrust vector. As described earlier, the centroid location is determined by the intersection of the angular measurement for maximum intensity of each probe. The collected current intensity for each probe was recorded as a function of angular position on an X-Y recorder. One set of probe scans is shown in Fig. 29 for a beam current I_B = 67 mA. Each of the vertical lines on the curves represents 5°. Data were obtained for north, south, east, and west thrust-vector deflections. These directions are referenced to facing the thruster as shown in Fig. 23. In the DGVS, the deflected beam moves in the direction opposite to the direction of the accel grid movement. During the checkout of the actuators, it was observed that the motor drives often stepped when switching from one motor to the other. This stepping could be either at zero or ± 1 counts depending on step location. This effect was normally eliminated by switching the motors only at locations of zero stepping. A continuity switch was employed at the end-of-travel of each actuator to locate the accel-position corresponding to a given motor step count. The data were analyzed by plotting the centroids of the thrust vectors as measured by the probes. These were then referenced to what was considered to be the undeflected vector by a series of concentric circules that represent integral number of degrees. The analysis is more apparent by looking at Fig. 30 for a beam current I_B = 50 mA. The N-S and E-W centroid deflections in Fig. 30 are represented by the numbered circles and squares, respectively. The numbers correspond to the position of the accel grid over the deflection range. Maximum deflections for E-W

ION BEAM COLLECTION CURRENT, RELATIVE MAGNITUDE

3448-15R1

ACCEL POS = 12 (E-W)

V_B = 1200 V

V_{AC} = 300 V

I_B = 67 mA

I_{AC} = 0.5 mA

ANGULAR INCREMENTS OF 5°
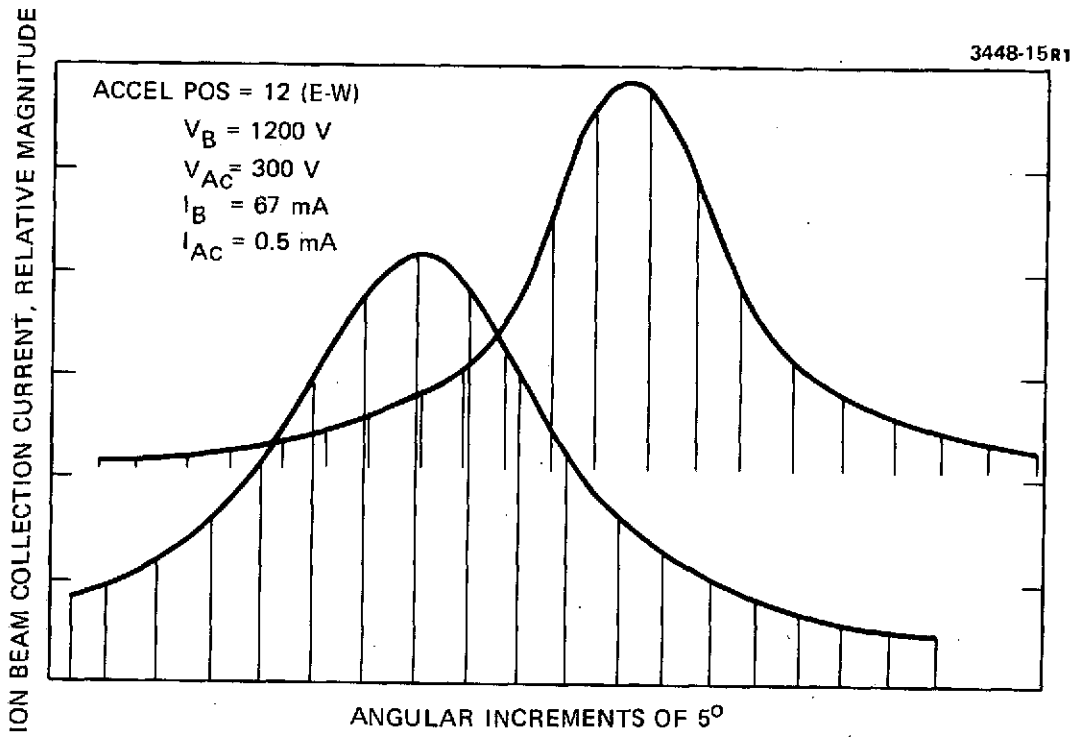
Fig. 29. Probe scans for a beam current, I_B = 67 mA.

Fig. 30. Centroid measurements 47.2 cm from accel grid.
(N-S centroid deflections are represented by
numbered circles, and E-W deflections are
represented by numbered squares.)

movement are 0 and 12, while 0 and 11 indicate the maximums for N-S. Figure 30 shows that the thrust vector can be deflected in N-S or E-W directions a total angle of about 14°.* There is some nonlinearity with respect to the deflection angle and motor counts. Figure 31 shows a similar set of data for a beam current I_B = 67 mA. The deflection angles here are similar to those in Fig. 30. The data in Fig. 31 also illustrate how the N-S motor was pulsed while switching to the E-W motor. There are also some indications that unwanted electrical command impulses were received by the actuators during the taking of data at points ③ and ⑥ in Fig. 31. Figure 32 shows the results for a beam current I_B = 32 mA beam and Fig. 33 shows the results for a beam current I_B = 67 mA at a lower net accelerating voltage. More will be said about these data in the paragraphs below.

TABLE XIV

Thruster Operation Setpoints

V_B, V	V_{Ac}, V	I_B, mA
1200	-300	70
1200	-300	50
1200	-300	33
800	-200	65

T1363

Beam deflection angles were compared by considering only the endpoint data since these were the only positions known with certainty. The analysis assumed that the maximum deflection angles were symmetric about the thruster axis as shown in Fig. 33. This may not be precisely true but it will serve the needs of the analysis. Corresponding

---

*This deflection magnitude was only one-half the value expected on the basis of earlier studies described in Ref. 17. The difference may be attributed to the higher values of beam current density or to higher values of beam-to-total voltage ratio.
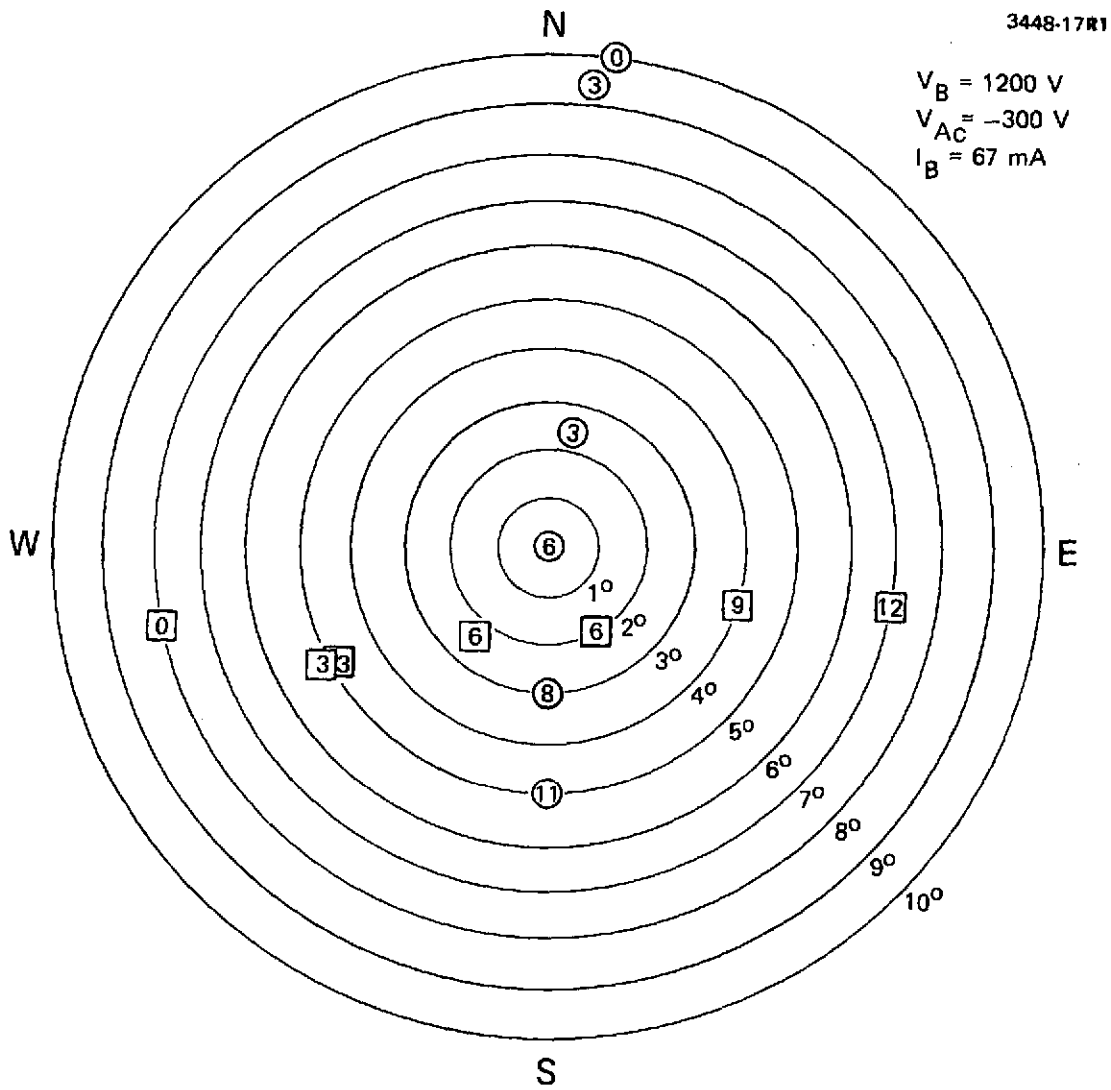
73

Fig. 31. Centroid measurements 47.2 cm from accel grid.

Fig. 32.   Centroid measurements 47.2 cm from accel grid.

Fig. 33.   Centroid measurements 47.2 cm from accel grid.

to the geometrical model shown in Fig. 34, the separation measured between the centroids of maximum plus and minus deflections is 2d at a distance D from the thruster. The deflection half angle θ for various settings using this analysis is shown in Table XV; the deflection angles are estimated to be accurate to within ±1 degree.

TABLE XV

Maximum Half Angle Deflections

V_B, V	V_{Ac}, V	I_B, mA	θ (East-West), Degrees	θ (North-South), Degrees
1200	-300	67	$7^\circ 21'$	$7^\circ 34'$
1200	-300	50	$7^\circ 18'$	$7^\circ 18'$
1200	-300	32	$7^\circ 8'$	$7^\circ 21'$
800	-200	67	$6^\circ 4'$	$7^\circ 2'$

T1364

Maximum deflection angles are not affected over the current and voltage values investigated in Table XV. The results in Table XV also show that the maximum deflection value expected for the DGVS is ±7°. The centroids measured along the E-W or N-S direction in Fig. 30 to 33 are in straight lines and the lines were orthogonal to within 5 to 15°. The difference from exact orthogonality is not understood, but was also detected on a lesser scale for the gimbaled thruster system.

The accel currents corresponding to the data of Figs. 30 through 33 are presented in Figs. 35 and 36 for the N-S deflection and E-W deflection, respectively. The legend used in each of these figures is given below:
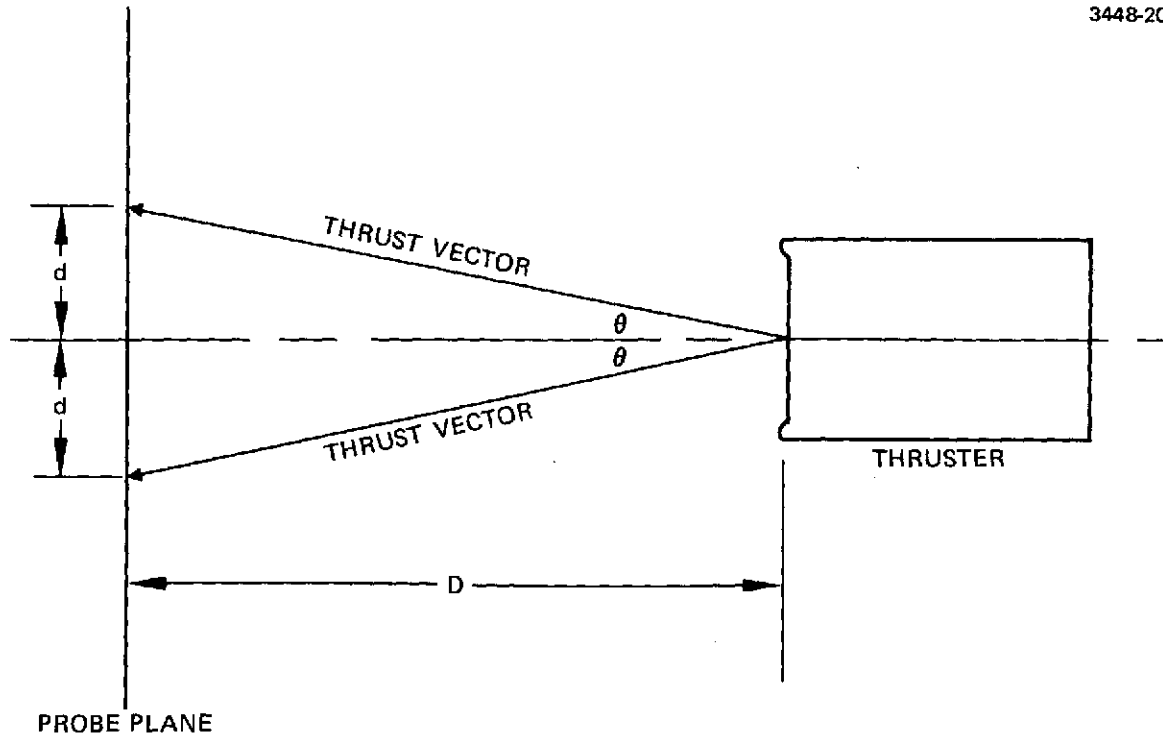
V_B = Beam voltage

V_{Ac} = Accel voltage

PROBE PLANE

Fig. 34. Model used for calculation of half angles.

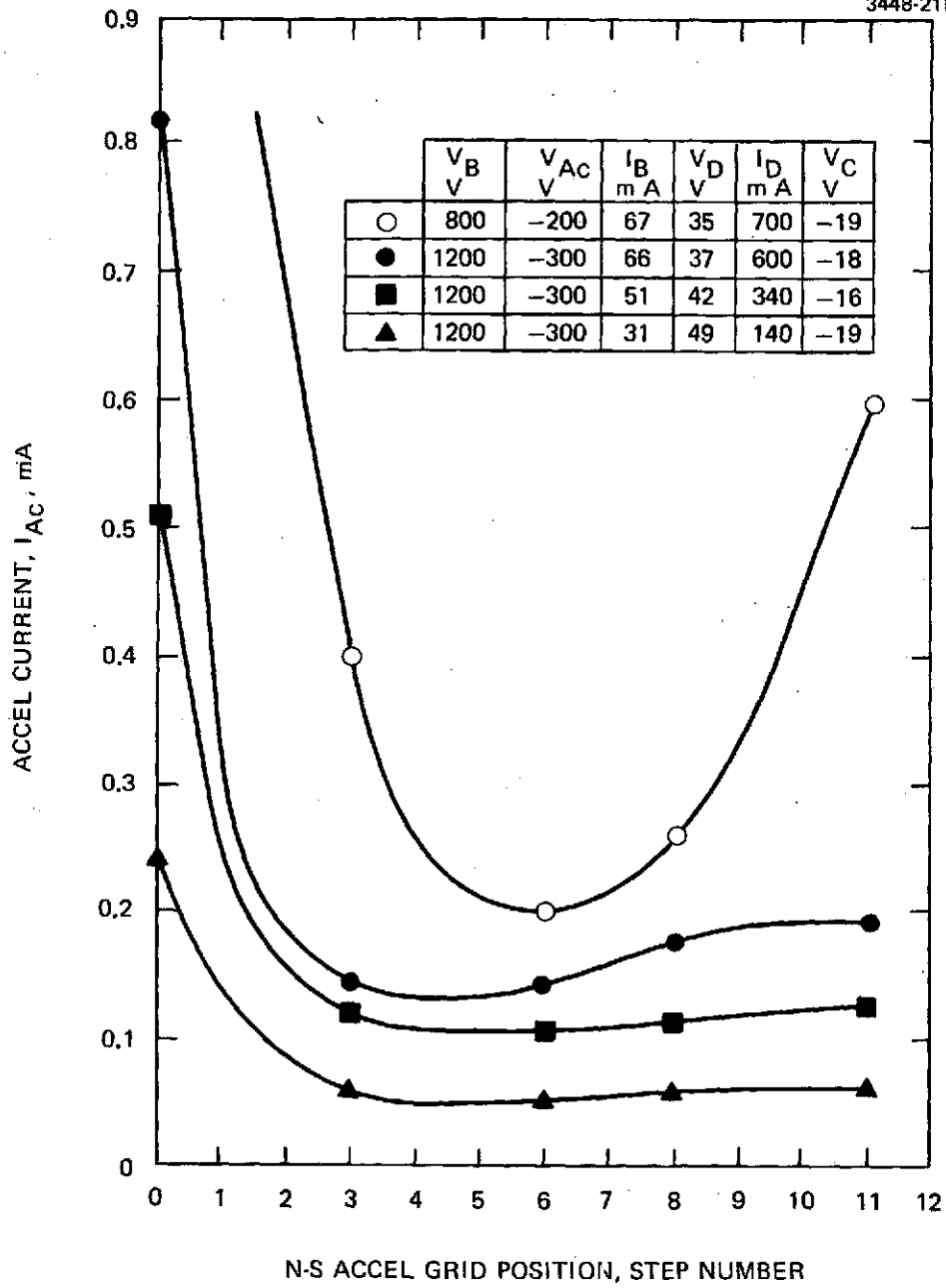|	V_B V	V_{Ac} V	I_B mA	V_D V	I_D mA	V_C V
○	800	−200	67	35	700	−19
●	1200	−300	66	37	600	−18
■	1200	−300	51	42	340	−16
▲	1200	−300	31	49	140	−19

N-S ACCEL GRID POSITION, STEP NUMBER

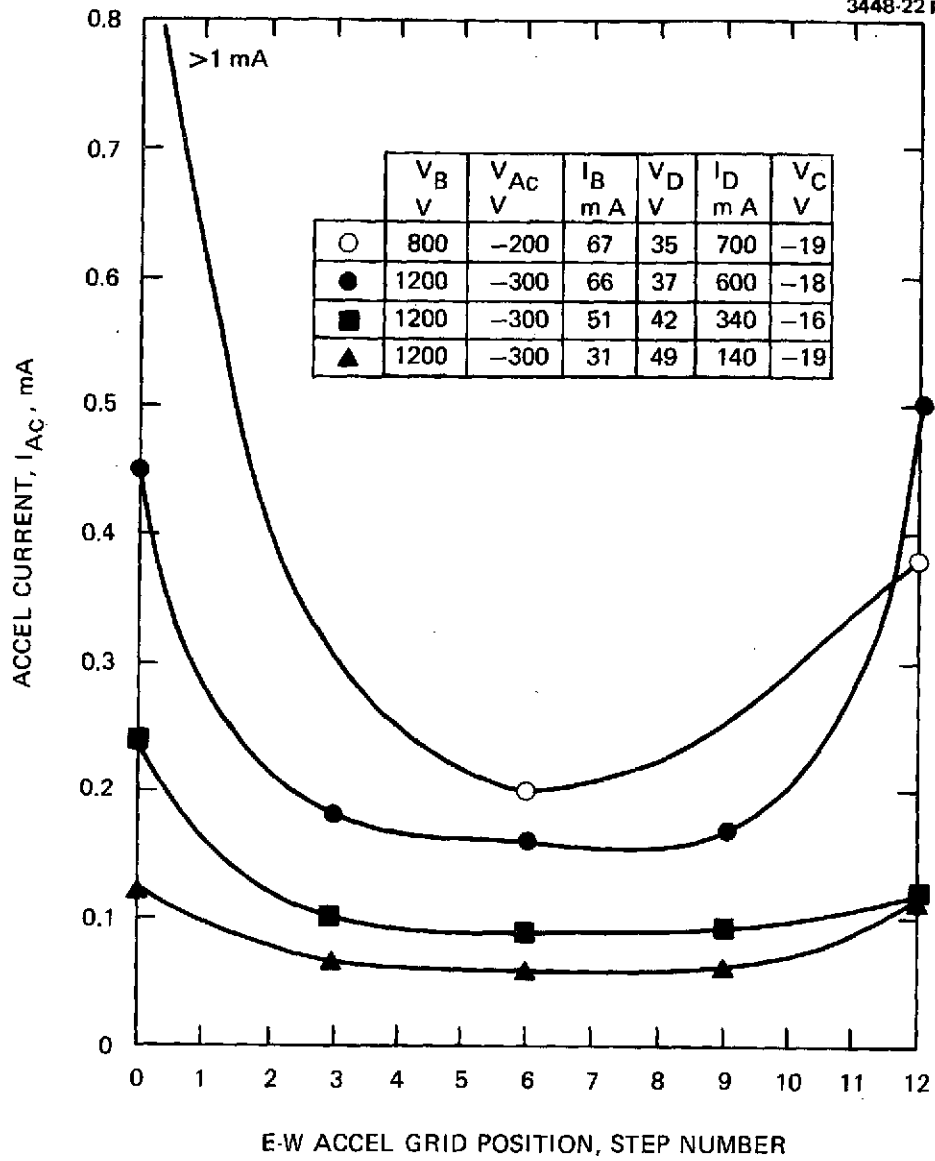Fig. 35.   Accel current versus accel N-S grid position.

Fig. 36. Accel current versus accel E-W grid position.

I_B = Beam current

V_D = Discharge chamber voltage

I_D = Discharge chamber current

V_C = Coupling voltage

In Fig. 35, positions, 0 and 11 are the maximum deflection positions while in Fig. 36 positions 0 and 12 are the maximum deflection positions. The accel current increases in all cases at these points and is dependent on the total beam current. The maximum measured values of interception are beyond the range which is desirable for a thrust vector deflection system.

I_B = 70 mA and I_B = 33 mA in the undeflection position. The divergence angle was obtained from probe scans at 7.9 cm and 47.2 cm from the accel grid. The scans for I_B = 70.5 mA are shown in Fig. 37. The divergent half angles are shown in Table XVI. At both beam levels, 90% of the beam is contained with a half-angle to less than 12°. The accuracy of the divergence measurements is estimated to be ±1 degree. When this is considered, the beam divergence is about the same for the measurements at beam current values I_B = 33 and I_B = 70.5 mA at the three intensity values presented in Table XVI. This is especially true for the angle which includes 90% of the beam.

TABLE XVI

Beam Divergence Half-Angles

V_B, V	V_{Ac}, V	I_B, mA	I_{Ac}, mA	Half Angles for Intensities of		
				50%	25%	10%
1200	-300	70.5	0.18	4.3°	7.3°	11.2°
1200	-300	33	0.07	6.3°	8.8°	11.8°

T1365

81

ION COLLECTION CURRENT, RELATIVE MAGNITUDE

3448-23R1

V_B = 1200 V
V_{Ac} = -300 V
I_B = 70.5 mA
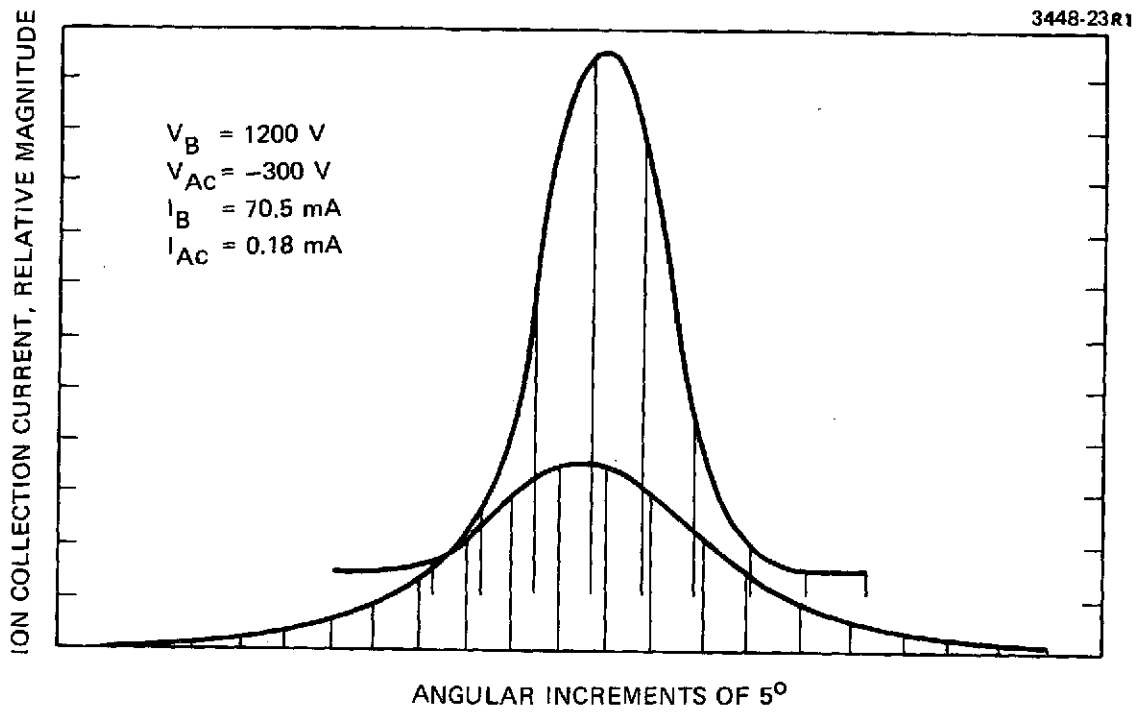I_{Ac} = 0.18 mA

ANGULAR INCREMENTS OF 5°

Fig. 37.   Beam profiles used for divergence measurements.

Beam divergence results in some loss of ion-beam thrust. The off-axis thrust component which results from beam divergence is azimuthally symmetric and cancels out thereby contributing nothing to the overall thrust level. The amount of ion-beam thrust loss due to beam divergence can be assessed from the measurements presented in Table XVI, but only in an approximate manner; the ion-beam current measured at very high angles cannot be identified with certainty as originating at the discharge-plasma interface, but may include charge-exchange ions generated far downstream of the beam-extraction system. To facilitate this assessment, the data of Table XVI are conservatively interpreted to imply that virtually the entire primary ion beam is contained within an envelope having a half-angle of 20°. If all beamlet divergence angles are assumed to be equally probable within this envelope, a thrust-loss correction of -2% is indicated.

SECTION III

SUMMARY OF RESULTS

Hughes has completed development of an 8-cm Structurally Integrated Ion Thruster (SIT-8) which extends the technology established in development of the SIT-5 thruster to include applications where higher thrust levels (one millipound or more) are required, and advances the level of component technology to assure the capability for thruster operation for accumulated beam-on times of 20,000 hours with a capability for 10,000 on-off duty cycles. A dished-grid beam-extraction system has been developed which is capable of remotely controlled misalignment between the screen and accel beam-forming apertures to provide a thrust vector capability of $\pm7^{\circ}$ in each of two orthogonal directions. A thruster gimbaling system has also been developed as an alternative approach to the beam-vectoring requirement; the thruster gimbaling system provides a $\pm10^{\circ}$ thrust vector capability. Both beam deflection systems have been designed for a capability of greater than 100,000 deflections.

REFERENCES

1. W. R. Hudson and B. A. Banks, "An 8-cm Electron Bombardment Thruster for Auxiliary Propulsion," AIAA Paper 73-1131, AIAA 10th Electric Propulsion Conference, Lake Tahoe, Nevada, October 31 through November 2, 1973.

2. R. L. Poeschel, "Experimental Mercury Ion Thruster," Final Report, Contract CSC-SS-290, Hughes Research Laboratories, Malibu, California (1972).

3. H. R. Kaufman, "Ion Thruster Propellant Utilization," Ph.D. Thesis, Department of Mechanical Engineering, Colorado State University (1971).

4. J. Hyman, Jr. and R. L. Peoschel, "Satellite Control Mercury Ion Thruster," AIAA Paper 73-1132, AIAA 10th Electric Propulsion Conference, Lake Tahoe, Nevada, October 31 through November 2, 1973.

5. S. Nakanishi and R. C. Finke, "A 9700-Hour Durability Test of a Five Centimeter Diameter Ion Thruster," NASA TMX-68284, Lewis Research Center, Cleveland, Ohio 44135.

6. R. L. Poeschel and W. Knauer, "A Variable Magnetic Baffle for Hollow Cathode Thrusters," Paper presented at AIAA 8th Aerospace Science Meeting, New York, January 1970.

7. E. G. Wintucky, "High Voltage Pulse Ignition of Mercury Discharge Hollow Cathodes," NASA TMX-7125, Lewis Research Center, Cleveland, Ohio 44135.

8. J. L. Power, "Sputter Erosion and Deposition in the Discharge Chamber of a Small Mercury Ion Thruster," NASA TMX-71424, NASA Lewis Research Center, Cleveland, Ohio 44135.

9. S. L. G. Askerov and L. A. Seva, "Cathode Sputtering of Metals by Slow Mercury Ions," Sov. Phys. -Solid State 11, 1288 (1969).

10. G. K. Wehner, "Sputtering Yields of Normally-Incident Hg^+ Ion Bombardment at Low Ion Energy," Phys. Rev. 108, 35 (1957).

11. W. R. Hudson and A. J. Weigand, "Hollow Cathodes with BaO Impregnated Porous Tungsten Inserts and Tips," NASA TM X-71417, Lewis Research Center, Cleveland, Ohio 44135.

12. J. Hyman, Jr., "Performance Optimized Small Structurally Integrated Ion Thruster System," Final Report NAS 3-15483, NASA CR-121183, May 1973, Hughes Research Laboratories, Malibu, CA 90265.

13. J. Hyman, Jr., "Design and Development of a Small Structurally Integrated Ion Thruster System," Final Report NAS 3-14129, NASA CR-120821, Oct. 1971, Hughes Research Laboratories, Malibu, CA 90265.

14. "Flexural Pivot Brochure," Bendix Corporation, Utica Division, Utica, N.Y.

15. T. Spalvins, "Lubrication with Sputtered MoS_2 Films," <u>ASLE Transactions</u> <u>14</u> 4, p. 267 (1971).

16. W. H. Kohl, <u>Handbook of Materials and Techniques for Vacuum Devices</u>, Reinhold Publishing Corporation, New York, New York.

17. H. J. King, et al., "Thrust Vectoring Systems Part I — 5 cm Systems," Final Report NASA Contract NAS 3-14058, Hughes Research Laboratories, Malibu, Calif. NASA CR-72877.